Supporting Online Material

Cleaning the Air and Improving Health With Hydrogen Fuel Cell Vehicles

[1]M. Z. Jacobson, [1]W.G. Colella, and [2]D.M. Golden

[1]Department of Civil and Environmental Engineering, Stanford University, Stanford, California 94305-4020, USA. Email: jacobson@stanford.edu

[2]Department of Mechanical Engineering, Stanford University, Stanford, California 94305-3032, USA.

Science, June 24, 2005

Introduction

This Online Supplementary Information (OSI) describes the model used for this study in more detail (Section 1), discusses the setup of simulations for the study (Section 2), discusses additional difference plots from the four cases examined (Section 3), provides details on the estimated cost analysis of hydrogen from wind power, discussed in the main text (Section 4), and provides estimates of the 100-year global warming potential of black carbon plus organic matter and of sulfur oxides (Section 5). The companion paper (*S1*) discusses the emission cases in detail and shows paired-in-time-and-space comparisons of baseline model predictions with data.

1. Description of the model.

The model used for this study was GATOR-GCMOM, a parallelized and one-way-nested global-through-micro-γ-scale Gas, Aerosol, Transport, Radiation, General Circulation, Mesoscale, and Ocean Model. The model treated time-dependent gas, aerosol, cloud, radiative, dynamical, ocean, and transport processes. Aerosol processes in each grid cell were treated among a single aerosol size distribution with 17 size bins and 13 components per bin. Cloud processes in each cell were treated among three hydrometeor distributions (liquid, ice, and graupel), each with 30 size bins and all the aerosol components plus liquid, ice, or graupel, in each bin. All processes described were solved in all grid cells in the stratosphere and troposphere. The model was parallelized with Message Passing Interface (MPI). All physical, chemical, and cloud, and radiative algorithms were parallelized by column. The model as a whole has been tested against meteorological, chemical, and radiative field data without nesting on urban scales (*S2-S5*), with nesting from the global-through-urban scale (*S6-S7*), with nesting from the global-through-regional scale (*S8*), without nesting on the freeway scale (*S9*), and on the global scale (*S10-S13*).

1.A. Atmospheric Dynamical and Transport Processes

On the global scale, the model solved the equations for momentum (under the hydrostatic assumption), thermodynamic energy, and total water with the potential-enstrophy, mass, and energy-conserving scheme of (*S14*). In nested regional grids, it solved with an enstrophy-, mass-, and kinetic-energy-conserving scheme (*S15*). Both modules used spherical and sigma-pressure coordinates in the horizontal and vertical, respectively. Transport of gases and aerosols is solved with the scheme of (*S16*) using online winds and vertical diffusion coefficients.

1.B. Gas Processes

Gas processes included emission, photochemistry, advection, turbulence, cloud convection of gases, nucleation, condensation onto and dissolution into aerosols, clouds, and precipitation, washout, and dry deposition. Gases affected solar and thermal-IR radiation, aerosol formation, and cloud evolution, all of which fed back to meteorology. Gas photochemistry was solved with SMVGEAR II (*S17*). The chemical mechanism included over 300 reactions relevant to urban, free tropospheric, and stratospheric chemistry. The mechanism is listed in (*S18*, Appendix Table B.4), but with some modified reaction rate coefficients from (*S19*).

1.C. Aerosol Processes

Aerosol processes were treated among 17 size bins and multiple aerosol components per bin. (*S20*) describes the numerical techniques for solving aerosol processes in the model. (*S21*) describes the techniques for solving interactions of aerosol particles with size-resolved hydrometeor distributions. Size- and distribution-dependent aerosol processes included emission, homogeneous nucleation, condensation, dissolution, aerosol-aerosol coagulation, aerosol-cloud/ice/graupel coagulation, equilibrium hydration of liquid water, internal-particle chemical equilibrium, irreversible aqueous chemistry, evaporation of cloud drops back to aerosol-particles, transport, sedimentation, dry deposition, rainout, and washout. Aerosols in the model affected solar and thermal-IR radiation, cloud evolution, gas concentrations, and surface albedo, all of which feed back to meteorology. The number concentration of particles and the mole concentrations of each component in each size distribution were prognostic variables. H_2SO_4-H_2O homogenous nucleation rates were calculated with the parameterization of (*S22*). Homogeneous nucleation was solved simultaneously with condensation of H_2SO_4-H_2O between the gas and all size bins of all distributions with a mass-conserving, noniterative, and unconditionally stable scheme (*S20*). The scheme was also used for condensation of organic gases onto size-resolved aerosols. The model also treated nonequilibrium dissolutional growth of inorganics (e.g., NH_3, HNO_3, HCl, H_2CO_3) and soluble organics to all size bins with a new mass-conserving nonequilibrium growth solver, PNG-EQUISOLV II (*S23*), where PNG is Predictor of Nonequilibrium Growth. EQUISOLV II (*S24*) is a chemical equilibrium solver that determines aerosol liquid water content, pH, and ion distributions following nonequilibrium growth. Aerosol-aerosol coagulation is solved among all distributions and components and among total particles in each bin with a volume-conserving, noniterative, algorithm (*S20*).

1.D. Gas-Aerosol-Cloud-Turbulence Interactions

The numerical techniques for cloud thermodynamics and microphysics are described predominantly in (*S21*). Cumulus and stratus clouds formed in the model by water growth onto 17 aerosol size bins to form liquid water drops or ice crystals or both. Following the growth calculation, the liquid drops and crystals were repartitioned from the 17-bin aerosol distribution into separate 30-bin liquid and ice hydrometeor distributions, where each bin contained all the chemical components of the underlying CCN aerosol particles. A third 30-bin hydrometeor distribution, graupel, was also tracked. This distribution formed upon heterocoagulation of the liquid water and ice hydrometeor distributions, contact freezing of aerosol particles with the liquid distribution, the heterogeneous-homogeneous freezing of the liquid distribution, and the evaporative freezing of the liquid distribution.

The water available for the original condensational/depositional growth calculation was determined with stratus and cumulus parameterizations. The stratus cloud scheme is from (*S25*) and was coupled with the calculation of turbulence (order 2.5). The stratus scheme predicted cloud fraction and cloud water content in each layer given turbulence terms and vertical gradients in potential temperature and moisture. Turbulence parameters affected clouds, momentum, energy, and tracers, particularly in the boundary

layer, which was resolved. Cumulus clouds were predicted with a modified Arakawa-Schubert algorithm (*S26*). In each column, nearly 500 subgrid cumulus clouds could form (and 1-10 typically formed), each defined by a unique cloud base and top (when 23 layers existed below the tropopause, 22 bases and 22 tops are possible). For each subgrid cloud, water and energy transport were solved with a mass-flux convection scheme; gas and size-resolved aerosol component transport were solved with a positive-definite, stable convective plume transport scheme. For each subgrid cloud, the model also generated adjustments to large-scale potential temperature, momentum, and water vapor.

Following cumulus-parameterization convection, the bulk water predicted in each layer from the cumulus and stratus parameterizations was evaporated/sublimated then regrown (simultaneously for liquid and ice) onto the size-resolved aerosol distributions transported to that layer. Because aerosols were transported vertically with cloud water in all cases, aerosol activation was consistent with that in a rising plume. The critical radius for liquid growth accounted for Raoult's law and the Kelvin effect and that for ice growth accounted for the Kelvin effect. In each size bin of each hydrometeor distribution, both effects were calculated based on the composition of the underlying aerosol material in the size bin, since such material was tracked. As such, changes in, for example, surface tension due to organics and inorganics were calculated based on the modeled composition of organics and inorganics in each cloud drop and ice crystal size bin.

Following growth, size-resolved processes treated were hydrometeor-hydrometeor coagulation (liquid-liquid, liquid-ice, liquid-graupel, ice-ice, ice-graupel, and graupel-graupel), aerosol-hydrometeor coagulation, large liquid drop breakup, settling, evaporative cooling during drop settling, evaporative freezing (freezing during drop cooling), heterogeneous-homogeneous freezing, contact freezing, melting, evaporation, sublimation release of aerosol cores upon evaporation/sublimation, coagulation of hydrometeors with interstitial aerosols, irreversible aqueous chemistry, gas washout, and lightning generation from size-resolved coagulation among ice hydrometeors. The coagulation kernel for all cloud interactions and aerosol-cloud interactions included a coalescence efficiency and collision kernels for Brownian motion, Brownian diffusion enhancement, turbulent inertial motion, turbulent shear, settling, thermophoresis, diffusiophoresis, and charge.

Aerosol particles of different size were removed by size-resolved clouds and precipitation through two mechanisms: nucleation scavenging and aerosol-hydrometeor coagulation. Both processes were size-resolved with respect to both aerosol particles and hydrometeor particles.

1.E. Radiative Processes

Radiation processes include UV, visible, solar-IR, and thermal-IR interactions with gases, size/composition-resolved aerosols, and size/composition-resolved hydrometeor particles. Radiative transfer is solved with the scheme of (*S27*). Calculations were performed over >600 wavelengths/probability intervals and affected photolysis and heating (*S28*). Gas absorption coefficients in the solar-IR and thermal-IR were calculated for H_2O, CO_2, CH_4, CO, O_3, O_2, N_2O, CH_3Cl, $CFCl_3$, CF_2Cl_2, and CCl_4, from HITRAN data (*S28*). Aerosol-particle optical properties were calculated assuming that BC (if present) comprised a particle's core and all other material coated the core. Shell real and imaginary refractive indices for a given particle size and wavelength were obtained by calculating the solution-phase refractive index, calculating refractive indices of non-solution, non-BC species, and volume averaging solution and nonsolution refractive indices. Core and shell refractive indices were used in a core-shell Mie-theory calculation (*S29*). Cloud liquid, ice, and graupel optical properties for each hydrometeor size and radiation wavelength were also determined from Mie calculations that accounted for absorbing inclusions. For such a calculation, nonspherical ice crystals were assumed to be

a collection of spheres of the same total volume to area ratio and total volume (*S30*). The surface albedos of snow, sea ice, and water (ocean and lake) were wavelength-dependent and predicted by (rather than specified in) the model (*S13*). Column calculations treat shading by structures (e.g., buildings) and topography.

1.F. Subgrid Surfaces and Oceans

The model treated ground temperatures over subgrid surfaces (up to 12 soil classes and roads over soil, roofs over air, and water in each cell). It also treated vegetation over soil, snow over bare soil, snow over vegetation over soil, sea-ice over water, and snow over sea-ice over water (*S6*). For all surfaces except sea ice and water, surface and subsurface temperatures and liquid water were found with a time-dependent 10-layer module. Ocean mixed-layer velocities, energy transport, and mass transport were calculated with a gridded 2-D potential-enstrophy, energy, and mass-conserving shallow-water equation module, forced by wind stress (*S31*), based on the shallow-water scheme of (*S14*). The actual depth at each location was a prognostic variable, but because the module conserved volume exactly, the average mixing depth over the global ocean was constant (80 m). For lake water, a fixed 80 m mixing depth was assumed. Water (ocean and lake) temperatures were also affected by sensible, latent, and radiative fluxes. Nine additional layers existed below each ocean mixed-layer grid cell to treat energy diffusion from the mixed layer to the deep ocean and ocean chemistry. Dissolution of gases to the ocean and ocean chemistry were calculated with a new scheme, OPD-EQUISOLV O (*S32*), where OPD is solver of nonequilibrium transport between the ocean and atmosphere and EQUISOLV O solves chemical equilibrium in the ocean. Both schemes are mass conserving and unconditionally stable.

2. Discussion of the Simulations

For the present study, the model was run for August 1999. 1999 was chosen for the baseline because a detailed inventory was available for that year. August was chosen since it is a month of typical smog events. Two one-way nested grids were used: a global grid (4°-SN x 5°-WE resolution), and a U.S. grid (0.5°S-N x 0.75°W-E or about 55 km S-N x 68 km W-E resolution). The global grid treated 39 sigma-pressure layers between the surface and 0.425 hPa. The regional grid included 26 layers between the surface and 103.5 hPa, matching the 26 bottom layers of the global grid. Each grid included five layers in the bottom 1 km. The nesting time interval for passing meteorological and chemical variables was one hour. Variables passed at the horizontal boundaries included temperature, specific humidity, wind velocity, gas concentrations, and size- and composition-resolved aerosol concentrations.

U.S. emission data for the baseline case were obtained from the U.S. National Emission Inventory (*S33*), which treats 370,000 stack and fugitive sources, 250,000 area sources, and 1700 categories of onroad and nonroad vehicular sources (including motorcycles, passenger vehicles, trucks, recreational vehicles, construction vehicles, farm vehicles, industrial vehicles, etc.). Pollutants emitted hourly included CO, CO_2, H_2, H_2O, CH_4, speciated NMOGs (paraffins, olefins, formaldehyde, higher aldehydes, toluene, xylene, isoprene, monoterpenes), NO, NO_2, HONO, NH_3, SO_2, SO_3, H_2SO_4 and speciated particulate black carbon, organic carbon, sulfate, nitrate, and other. Emission inventories for each of three hydrogen cases (steam-reforming of natural gas, wind, and coal gasification) and a hybrid case were prepared following a life cycle assessment (LCA) that accounted for energy inputs and pollution outputs during all stages of hydrogen and fossil-fuel production, distribution, storage, and end-use, as described in (*S1*). Table S1, below, shows the summed yearly-averaged baseline emission and the differences in emission from the baseline case for each of the four cases, as described in the Table caption. The changes in Table S1 represent changes to vehicle, power plant, and other emission due to changes to a hydrogen- or hybrid-based economy. For example, emissions due to power for compressing hydrogen in all HFCV cases and for gasifying

coal in the coal case were added proportionally to the power plant emission mix in the inventory without changing the number of power plants or their control technologies. The main text summarizes the changes descriptively. (*S1*) details them quantitatively with equations and explanations of the underlying assumptions.

Table S1. Speciated yearly-averaged baseline (1999) emission (metric tonnes/yr) from all U.S. anthropogenic sources, obtained from the U.S. National Emission Inventory, and the emission differences between the inventories derived for each model sensitivity experiment (Tables 5-8 of (*S1*)). and the baseline inventory.

Species	Baseline emission (tonnes/yr)	Hybrid -baseline (tonnes/yr)	Natural gas -baseline (tonnes/yr)	Wind -baseline (tonnes/yr)	Coal -baseline (tonnes/yr)
Gases					
Carbon monoxide (CO)	1.12×10^{8}	-1.92×10^{7}	-6.18×10^{7}	-6.18×10^{7}	-5.82×10^{7}
Nitrogen oxides as NO_2	2.19×10^{7}	-2.35×10^{6}	-7.27×10^{6}	-7.28×10^{6}	-7.12×10^{6}
Organics (NMOC+CH_4)					
Paraffins	1.40×10^{7}	-1.09×10^{6}	-3.80×10^{6}	-3.80×10^{6}	-3.80×10^{6}
Olefins	5.21×10^{5}	-4.98×10^{4}	-1.69×10^{5}	-1.69×10^{5}	-1.69×10^{5}
Ethene	9.12×10^{5}	-7.05×10^{4}	-2.27×10^{5}	-2.27×10^{5}	-2.27×10^{5}
Formaldehyde	2.23×10^{5}	-1.38×10^{4}	-4.38×10^{4}	-4.39×10^{4}	-4.37×10^{4}
Higher aldehydes	3.39×10^{5}	-5.34×10^{4}	-1.76×10^{5}	-1.76×10^{5}	-1.76×10^{5}
Toluene	2.60×10^{6}	-1.02×10^{5}	-4.35×10^{5}	-4.35×10^{5}	-4.34×10^{5}
Xylene	2.25×10^{6}	-1.45×10^{5}	-6.22×10^{5}	-6.22×10^{5}	-6.22×10^{5}
Isoprene	9.92×10^{3}	-1.51×10^{3}	-4.91×10^{3}	-4.91×10^{3}	-4.91×10^{3}
Total NMOC	2.09×10^{7}	-4.36×10^{5}	-1.68×10^{6}	-1.68×10^{6}	-1.68×10^{6}
Methane (CH_4)	6.31×10^{6}	-2.45×10^{5}	1.32×10^{6}	-8.05×10^{5}	-8.04×10^{5}
Sulfur oxides as SO_2	1.81×10^{7}	-8.67×10^{4}	3.70×10^{5}	3.70×10^{5}	9.70×10^{5}
Ammonia	4.53×10^{6}	-7.39×10^{4}	-2.38×10^{5}	-2.38×10^{5}	-2.38×10^{5}
Hydrogen	3.18×10^{6}	-5.44×10^{5}	4.55×10^{6}	4.55×10^{6}	4.65×10^{6}
Carbon dioxide (CO_2)	5.30×10^{9}	-3.16×10^{8}	-7.96×10^{8}	-1.24×10^{9}	-6.20×10^{7}
Water vapor	1.99×10^{9}	-1.20×10^{48}	4.00×10^{7}	4.00×10^{7}	4.00×10^{7}
$PM_{2.5}$					
Organic matter	2.64×10^{6}	-1.55×10^{4}	-4.70×10^{4}	-4.70×10^{4}	-4.60×10^{4}
Black carbon	5.92×10^{5}	-2.82×10^{4}	-8.92×10^{4}	-8.92×10^{4}	-8.87×10^{4}
Sulfate	3.10×10^{5}	-6.02×10^{2}	-1.00×10^{3}	-1.00×10^{3}	-7.00×10^{2}
Nitrate	2.67×10^{4}	-7.13×10^{1}	-2.20×10^{2}	-2.20×10^{2}	-2.10×10^{2}
Other	8.26×10^{6}	-7.90×10^{3}	-1.20×10^{4}	-1.20×10^{4}	-7.00×10^{3}
Total $PM_{2.5}$	1.18×10^{7}	-5.23×10^{4}	-1.49×10^{5}	-1.49×10^{5}	-1.43×10^{5}
PM_{10}					
Organic matter	5.77×10^{6}	-2.29×10^{4}	-6.80×10^{4}	-6.80×10^{4}	-6.60×10^{4}
Black carbon	9.62×10^{5}	-3.32×10^{4}	-1.05×10^{5}	-1.05×10^{5}	-1.04×10^{5}
Sulfate	4.91×10^{5}	-9.24×10^{2}	-1.70×10^{3}	-1.70×10^{3}	-1.20×10^{3}
Nitrate	7.10×10^{4}	-1.01×10^{2}	-2.70×10^{2}	-2.70×10^{2}	-2.60×10^{2}
Other	3.75×10^{7}	-9.16×10^{3}	-1.00×10^{4}	-1.00×10^{4}	0.00×10^{0}
Total PM_{10}	4.48×10^{7}	-6.63×10^{4}	-1.84×10^{5}	-1.84×10^{5}	-1.71×10^{5}

NMOC is nonmethane organic carbon. $PM_{2.5}$ and PM_{10} are particulate matter smaller than 2.5 μm and 10 μm in diameter, respectively.

Biogenic emission of biogenic isoprene, monoterpenes, other VOCs, and NO for North America were derived from 1-km vegetation and land-use data from the third generation Biogenic Emissions Landuse Database (BELD3) (*S34*) and for the rest of the world from USGS 1-km landuse/landcover data (*S35*). A program was written to produce

normalized (at a specific temperature and radiation level) inventories of biogenic isoprene, monoterpenes, other VOCs, and NO emission from these data (which include vegetation categories and emission factors for each landuse type) for any spatial and temporal grid. Normalized data were combined in the model with temperature- and radiation-dependent correction factors from (*S36*) to derive emission rates affected by the current temperature and radiation fields.

Emission of anthropogenic black carbon (BC) and organic matter outside the U.S. were obtained from (*S37*). Emission of biomass burning, sea spray, soil dust, lightning NO, ocean DMS, volcanic SO_x, and other global sources of NO_x, SO_x, NH_3, CH_4, CO, N_2O, organics, and CO_2 are described in (*S12,S13*).

Initial meteorological fields for both domains were obtained from National Center for Environmental Prediction (NCEP) reanalysis fields for August 1, 1999, at 12 GMT (*S38*). No data assimilation, nudging, or model spinup was performed during any simulation. Aerosol and gas fields in both domains were first initialized from background data, then overridden over the U.S. for O_3, CO, NO_2, SO_2, $PM_{2.5}$, and PM_{10} using U.S. EPA ambient air quality data (*S39*), interpolated from over 1650 stations to model grid cell at the time corresponding to initialization.

3. Simulation Results

Five numerical simulations were run for the month of August 1999: a baseline simulation, a simulation in which fossil-fuel onroad vehicles were converted to gasoline-electric hybrid vehicles, and three simulations in which fossil-fuel vehicles were switched to HFCV where the hydrogen was produced from (a) steam-reforming of natural gas, (b) wind energy, and (c) coal gasification. Emission changes for each scenario are detailed in (*S1*).

Figure S1*a-q* shows modeled differences, averaged over the month of August (day and night) in the mixing ratio or concentration of several gas and particle components, for each of the four cases (natural gas, wind, coal, hybrid). The figures were obtained by taking the difference between the baseline-case results, averaged every hour over a month, and the results from each of the respective cases, averaged every hour over a month.

Of the species plotted carbon monoxide, nitric oxide, nitrogen dioxide, toluene, sulfur dioxide, black carbon, nitrate, sulfate, water vapor, methane, carbon dioxide, and molecular hydrogen had emission sources and were affected by chemistry and/or other atmospheric processes. Nitric acid, ozone, PAN, the hydroxyl radical had no emission sources, but were produced and destroyed chemically.

Figure S1*a* shows that carbon monoxide reductions occurred in all four cases. The reductions were least in the hybrid case. About 55 percent of all CO emission in 1999 was due to onroad vehicles, so the elimination of gasoline/diesel combustion from such vehicles was expected to cause a larger reduction, regardless of the method of producing hydrogen, than a switch to hybrids.

Figures S1*b* and S1*c* show that nitric oxide and nitrogen dioxide reductions, respectively, were similarly greater in all HFCV cases than in the hybrid case. About 34 percent of all NO_x emission in 1999 was due to onroad vehicles. Of all NO_x emission, about 90 percent was NO and 10 percent was NO_2. The additional electric power required to compress hydrogen and gasify coal resulted in a relatively small increase in power-plant NO_x emission, but the increase was much smaller than the decrease due to the reduction due to eliminating onroad-vehicle NO_x (*S1*).

Figure S1*d* shows that nitric acid mixing ratios decreased in all four cases. Decreases were greatest in Southern California, where significant nitric acid usually forms due to high NO_x emission there.

Figure S1*e* shows that switching to HFCV decreased toluene significantly but switching to hybrids had a smaller effect. In Colorado, toluene emitted from a large non-vehicle source slightly increased because OH (Fig. S1*j*), the main toluene oxidant, decreased there.

Figure S1*f* shows the greater loss (and also greater gains) in near-surface ozone (a secondary pollutant) due to switching to HFCV relative to switching to hybrid vehicles. Figure S1*g* shows that the zonally-averaged near-surface ozone in the U.S. decreased significantly upon a switch to HFCV relative to hybrid vehicles.

PAN, a secondary pollutant, decreased to a greater extent in all HFCV cases than in the hybrid case (Fig. S1*h*), as discussed in the main text.

Sulfur dioxide (Fig. S1*i*) decreased in some locations due to lower vehicle emission of SO_2 or higher hydroxyl radical (OH) mixing ratios, but it increased in other locations due to higher power plant emission or lower hydroxyl radical (OH) mixing ratios. The hydroxyl radical (Fig. S1*j*) generally decreased in locations where SO_2 increased and vice versa.

Figures S1*k-m* show changes in near-surface particulate black carbon (BC), particulate nitrate, and particulate sulfate, respectively. All have primary emission sources. Nitrate and sulfate also have gas-to-particle conversion sources. Nitrate forms from oxidation of NO and NO_2. Sulfate forms from oxidation of SO_2. Converting to HFCV or hybrids reduced BC and nitrate significantly (less so for hybrids), but increased particulate sulfate in all cases, even in the hybrid case. In the case of HFCV, sulfate increased due to higher SO_2 emission from power plants that resulted from increased energy needed to compress hydrogen and/or gasify coal. SO_2 also increased in the northeastern U.S. in all cases due to the faster oxidation of SO_2 there (Fig. S1*i*). Oxidation in the model was calculated in both the gas and aqueous phase (in size-resolved aerosol particles and cloud drops). Faster oxidation occurred because OH was higher in the northeast in the HFCV and hybrid cases (Fig. S1*j*). Much of the higher particulate sulfate corresponded to a decrease in SO_2.

Figure S1*n* shows differences in ambient water vapor from the cases. Ambient water vapor is controlled primarily by natural sources and sinks (e.g., cloud formation, ocean/lake evaporation, transport). Because (1) the natural sources and sinks of water vapor are several orders of magnitude greater than are the vehicle sources of water vapor, (2) switching from FFOV to HFCV or hybrids resulted in almost no change in water vapor emission (main text), and (3) changes shown in Fig. S1*n* are not in urban areas where one might expect to see water vapor differences, the differences in Fig. S1*n* were due to feedbacks of changes in all pollutants to large-scale meteorology, including feedbacks to clouds, atmospheric stability, and pressure gradients.

Figure S1*o* shows differences in near-surface methane. Methane increased in the natural gas-HFCV case by up to 40 ppbv but decreased in the other HFCV cases by up to 25 ppbv. It decreased to a lesser extent in the hybrid case. Methane is a combustion product of petroleum, so it was expected to decrease in the wind- and coal-HFCV and hybrid cases. The current background mixing ratio of methane is about 1700 ppbv in 1999, about 900 ppbv of which is anthropogenic. Because of the long lifetime of methane (about 10 years), ambient methane changes are expected to increase over simulations longer than the present one (one month).

Figure S1*p* shows baseline and differences in near-surface carbon dioxide. The globally- and yearly-averaged background CO_2 in 1999 was about 367 ppmv, with an August value of around 365 ppmv. CO_2's overall lifetime is about 30-95 years, so its ambient mixing ratios are expected to change to a greater extent over a simulation period longer than the one month period simulated here. CO_2 decreased to the greatest extent in the wind case, followed by the natural gas, coal, and hybrid cases, respectively.

Figure S1*q* shows the change in ambient molecular hydrogen due to the four cases. Hydrogen increased in all HFCV cases (due to the assumed hydrogen leakage that exceeded the reduction in hydrogen from reduced fossil-fuel combustion) and decreased in the hybrid case (due to reduced fossil-fuel combustion). The fossil-fuel hydrogen emission rate was assumed to be 0.0285 kg-H_2 per kg-CO emitted (*S40*). The baseline hydrogen shows elevated values mostly in the eastern U.S. and Los Angeles due to hydrogen emission from fossil fuel vehicles. (*S40*) shows measurements in Harvard Forest, where microbial degradation of H_2 is likely high, of of up to 900 ppbv H_2.

Figure S1. Modeled baseline case and differences, averaged over all day and night hours of the month of August 1999, of several near surface parameters (except for one zonally-averaged figure). For each parameter, five panels are shown, representing the baseline case and differences between the baseline and (i) natural gas, (ii) wind, (iii) coal, and (iv) hybrid cases.

(a) Near-surface carbon monoxide

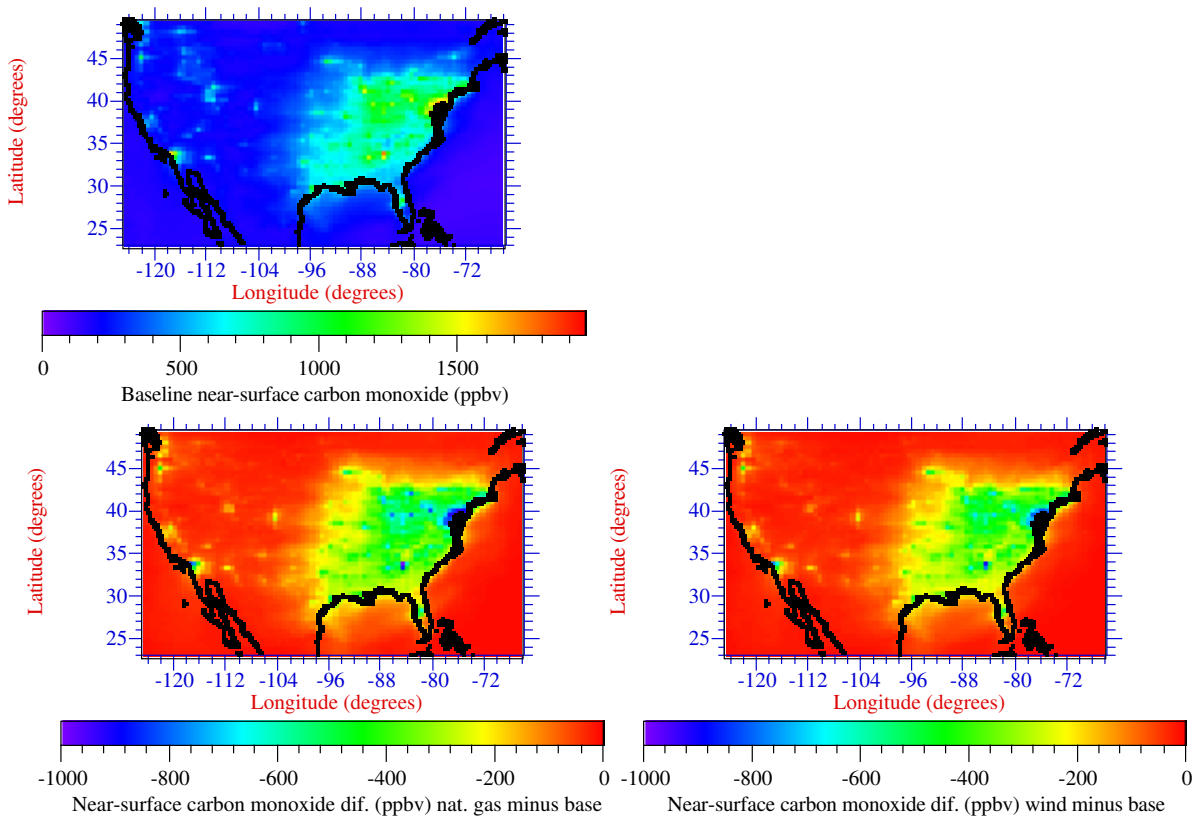

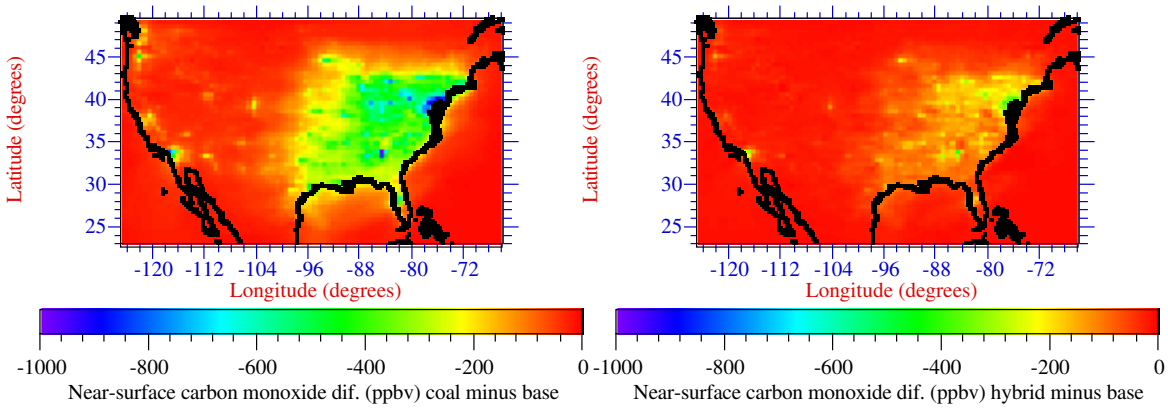

(b) Near-surface nitric oxide

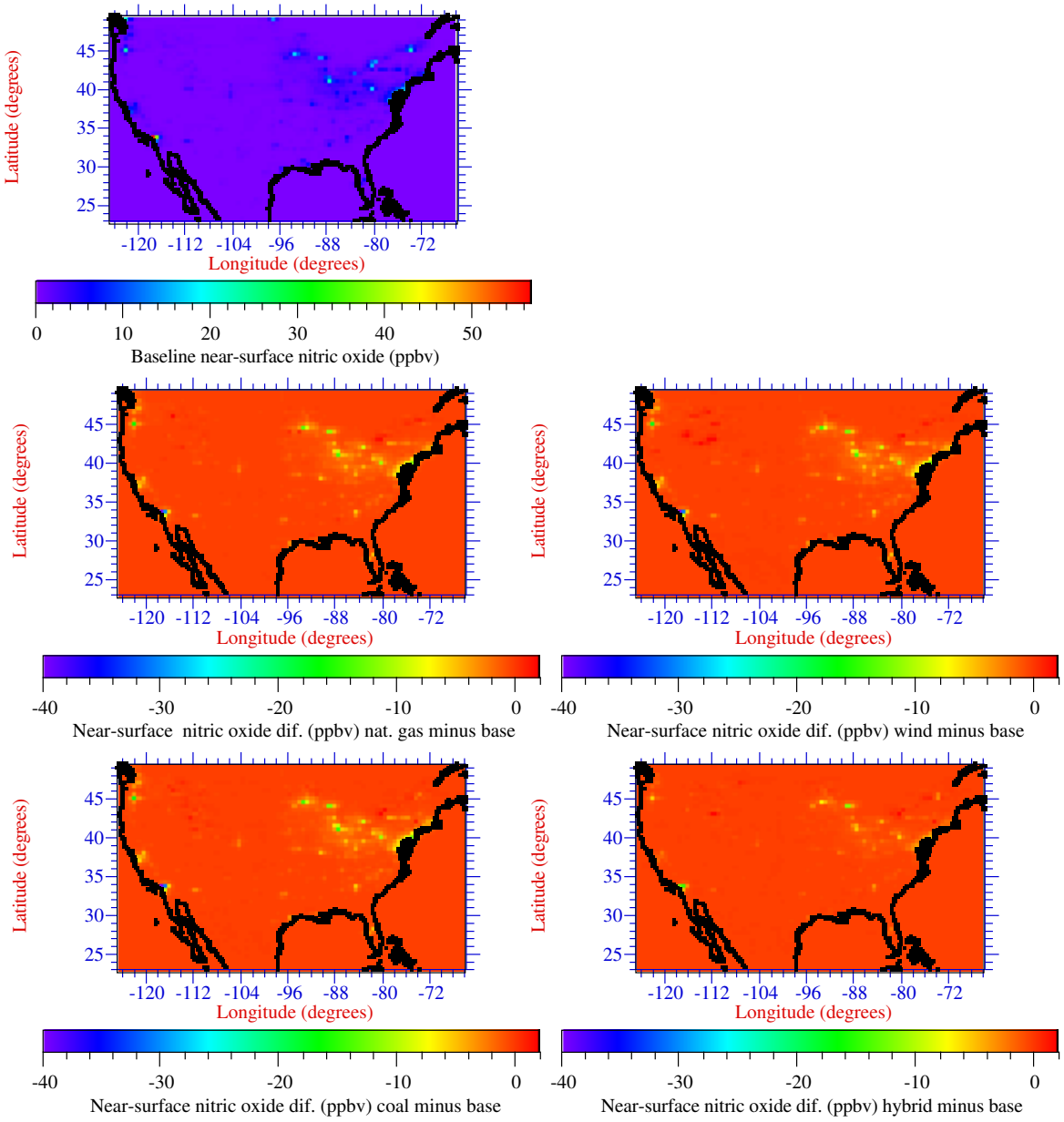

(c) Near-surface nitrogen dioxide

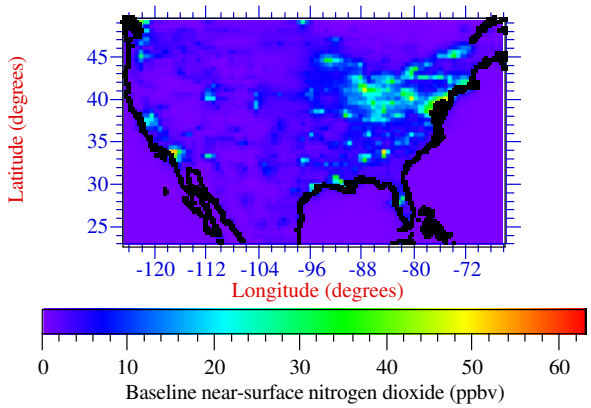

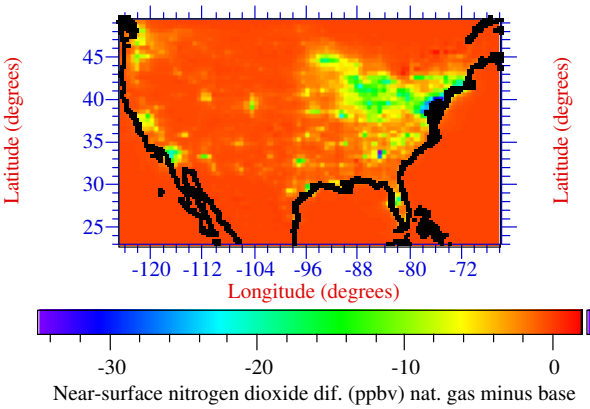

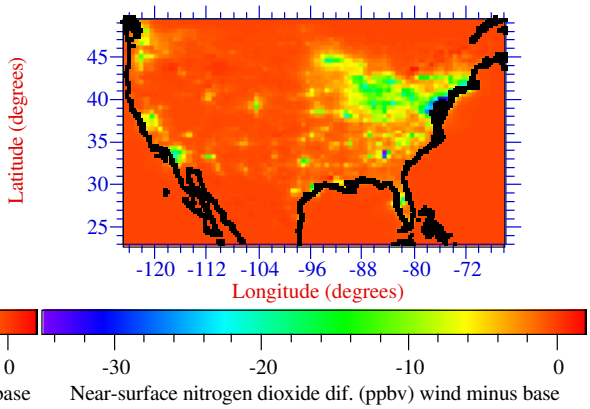

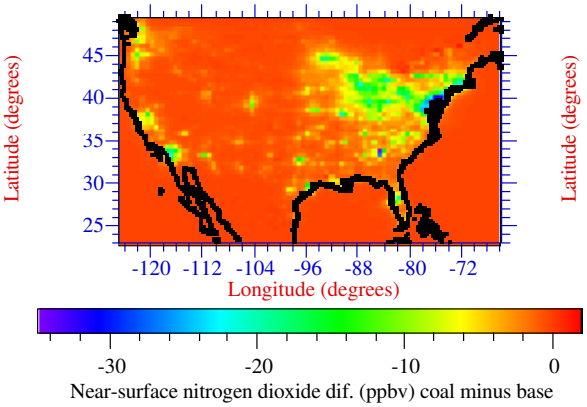

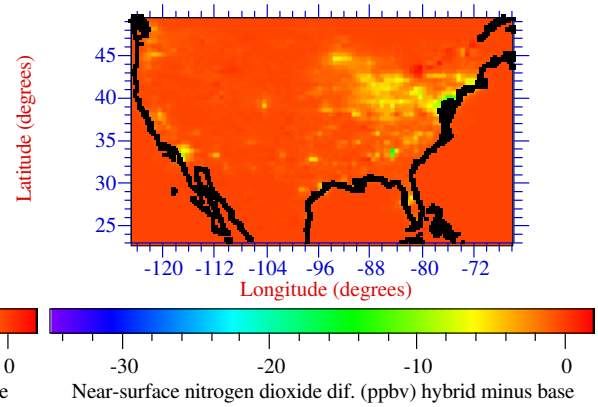

(d) Near-surface nitric acid

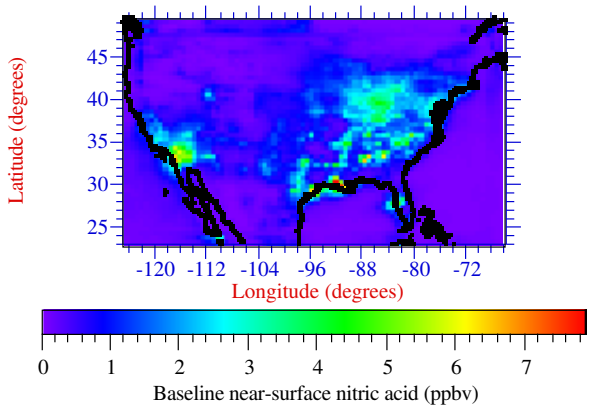

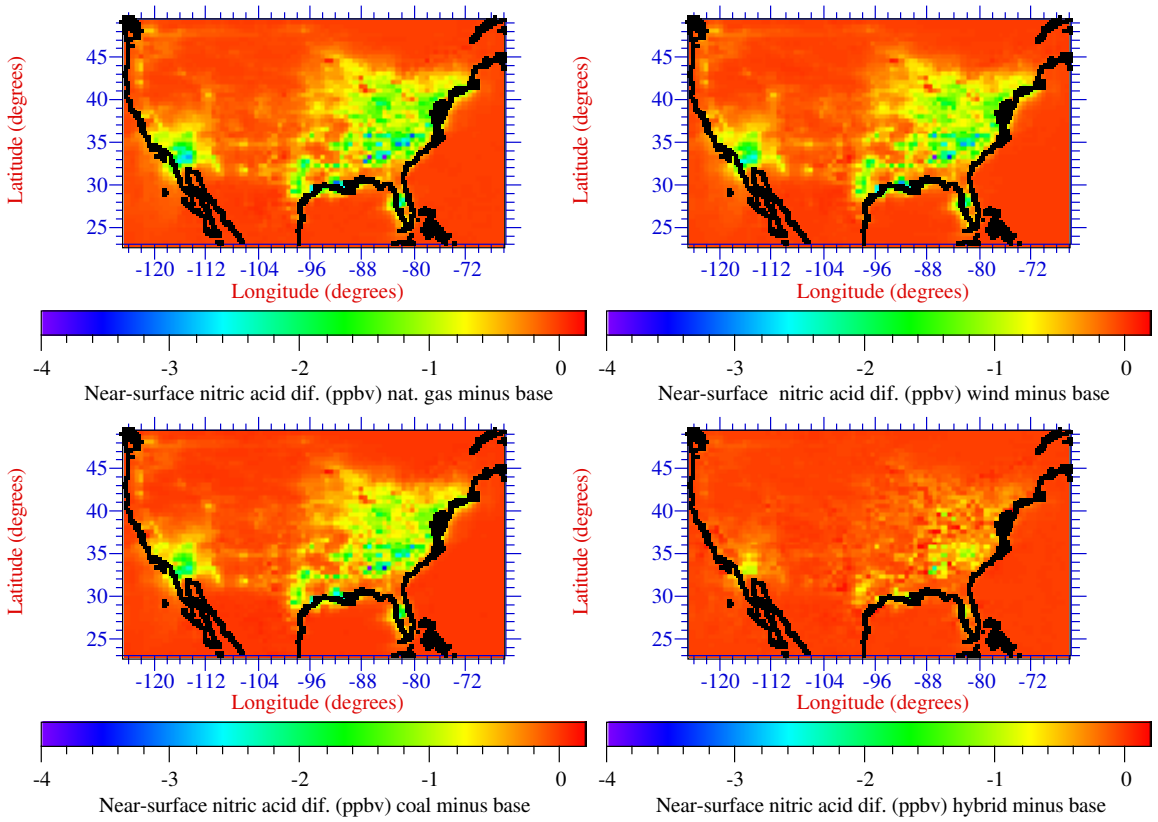

(e) Near-surface toluene

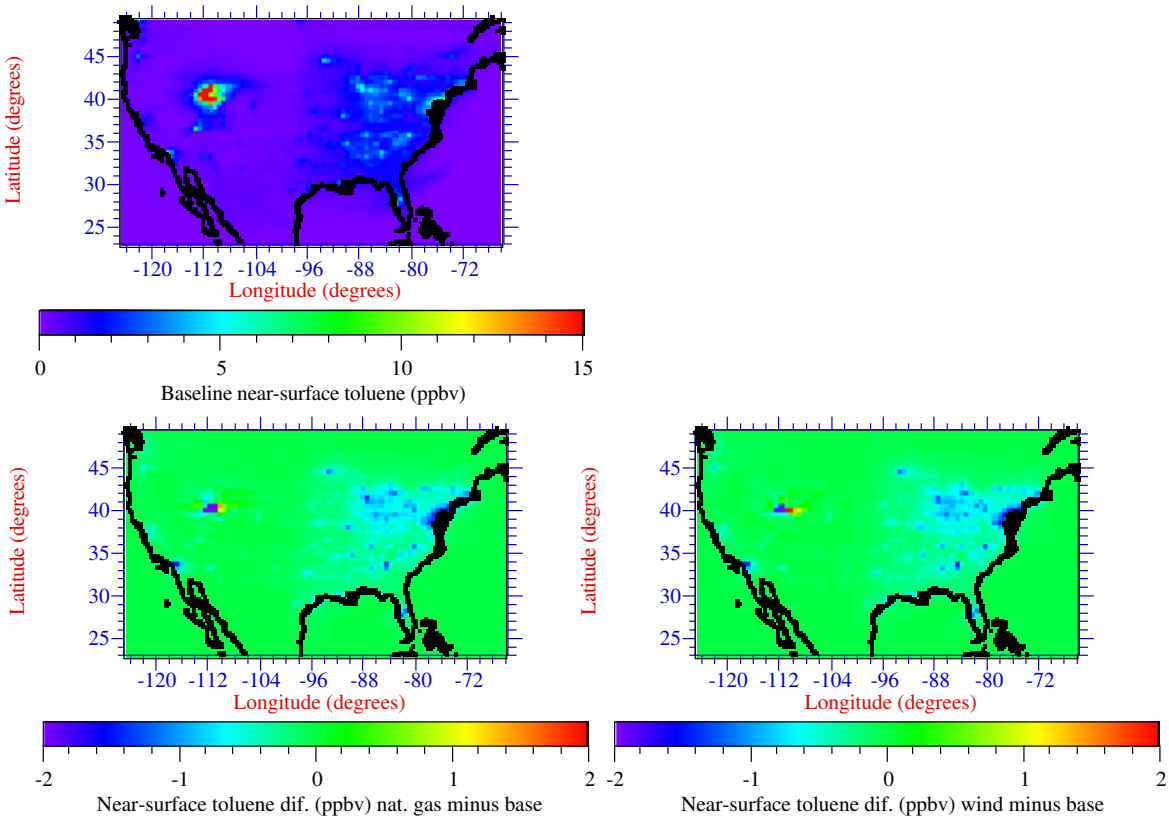

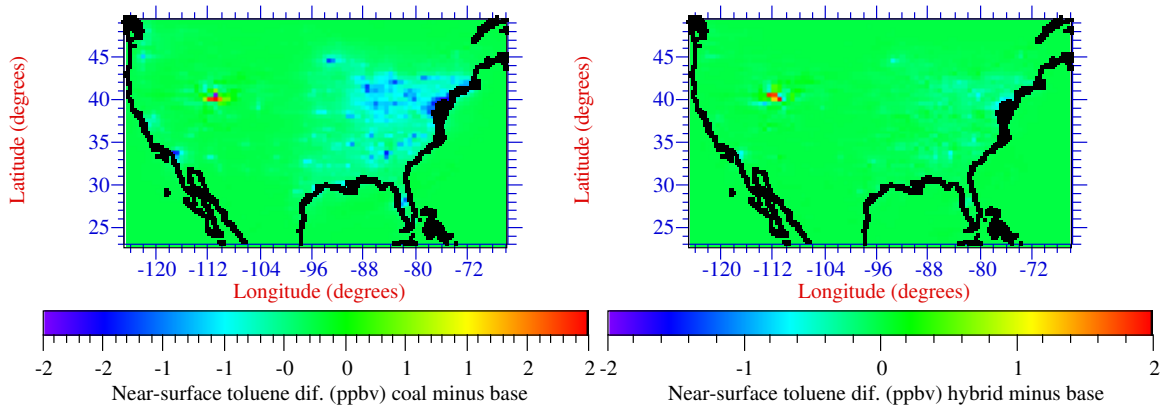

(f) Near-surface ozone

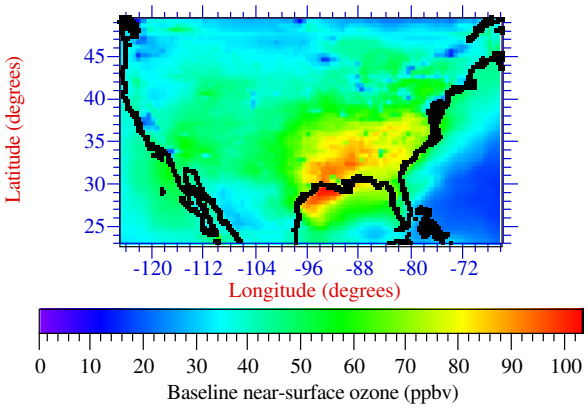

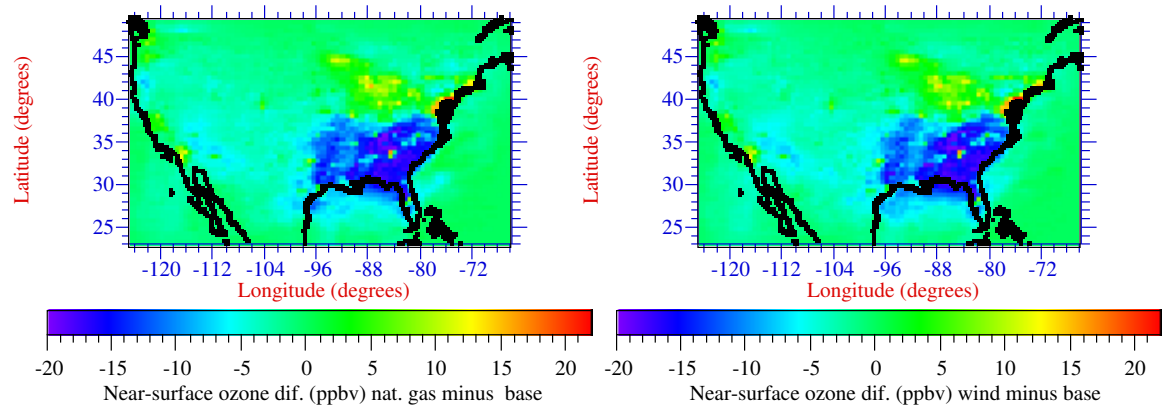

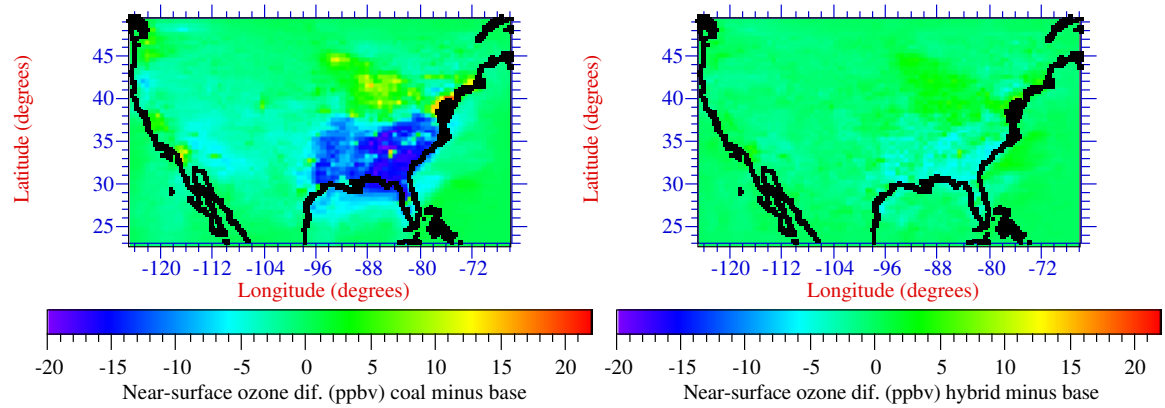

(g) Zonal ozone

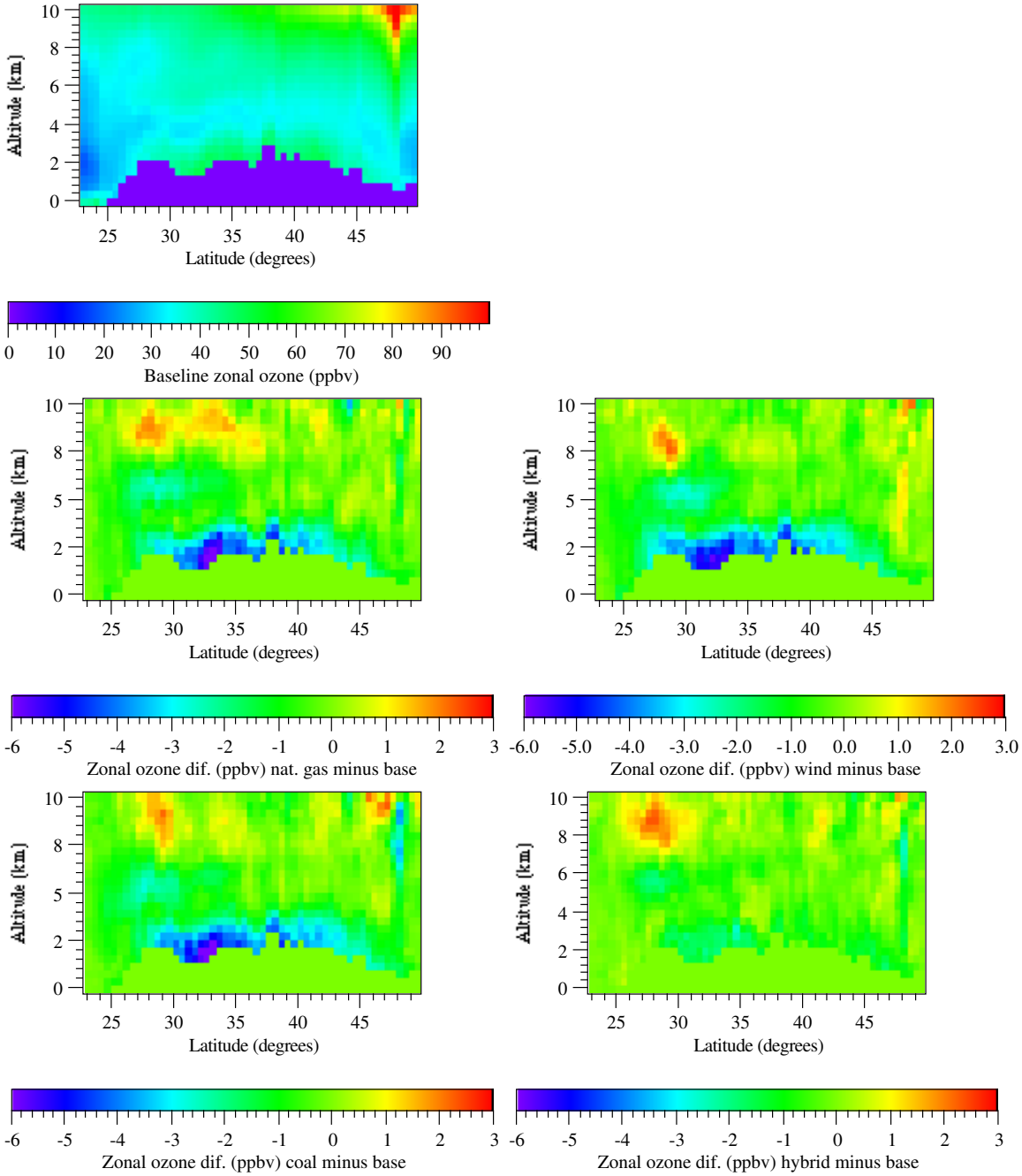

(h) Near-surface PAN

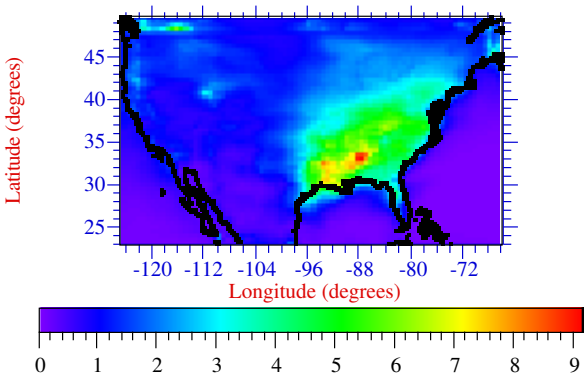

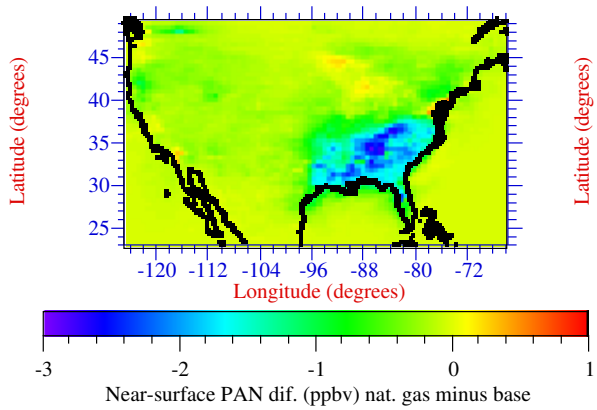

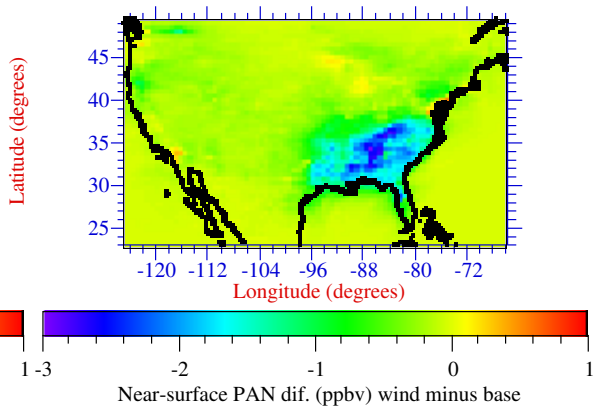

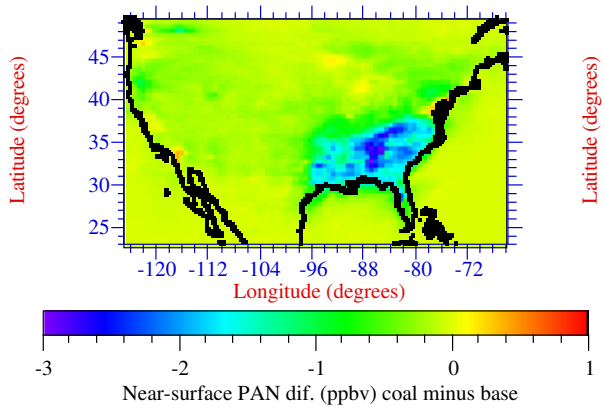

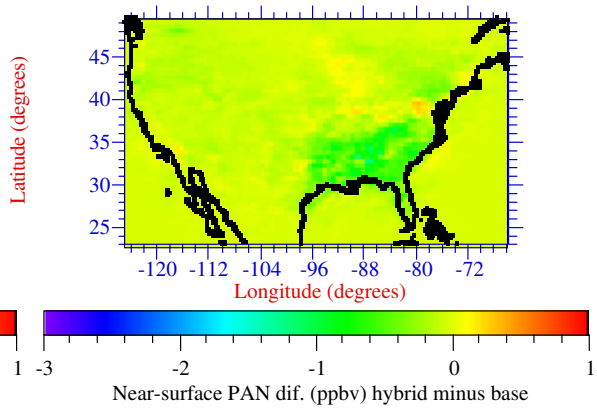

(i) Near-surface sulfur dioxide

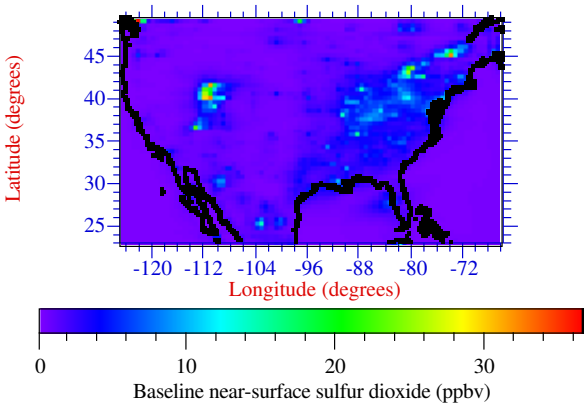

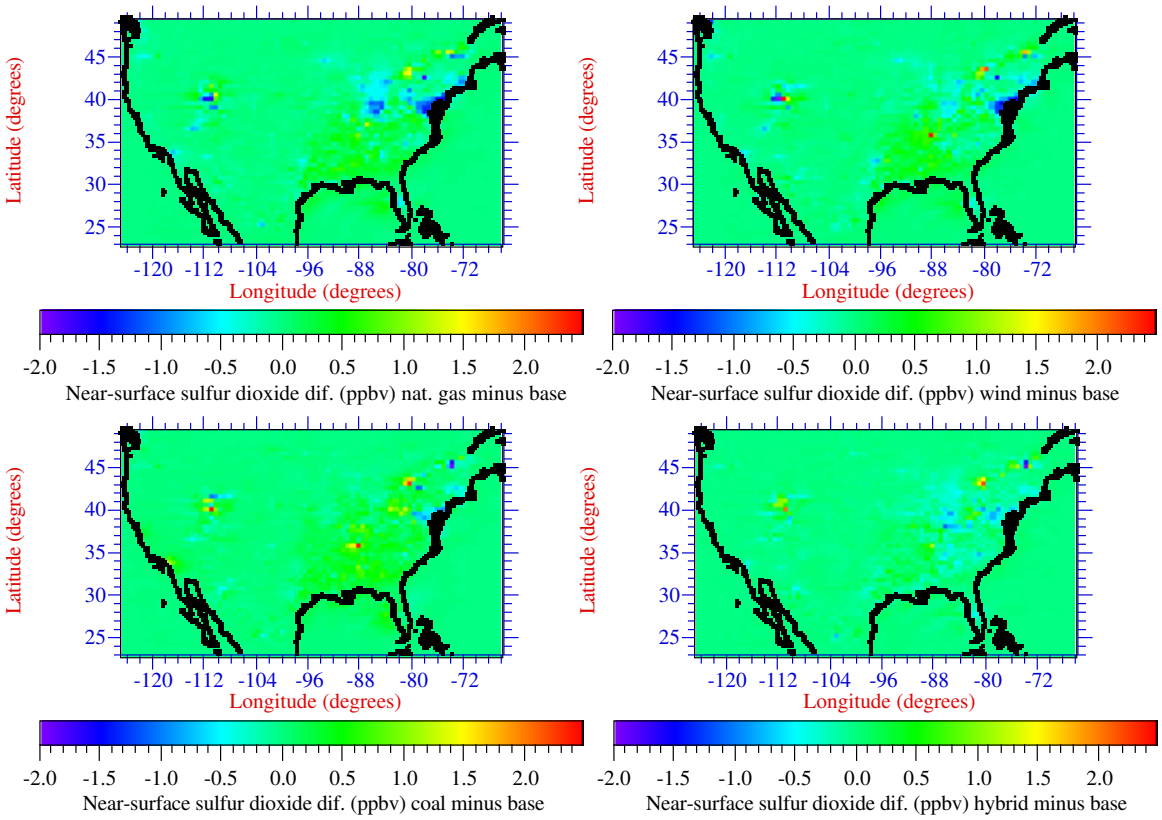

(j) Near-surface hydroxyl radical

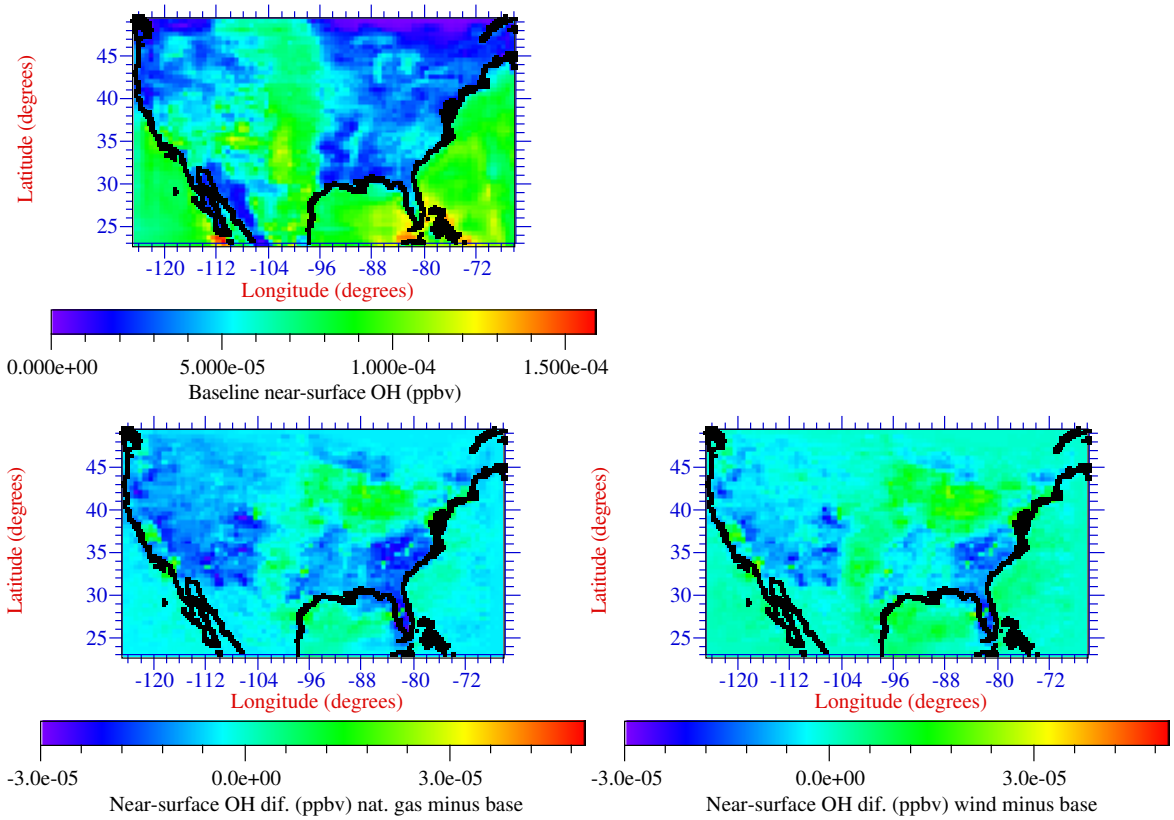

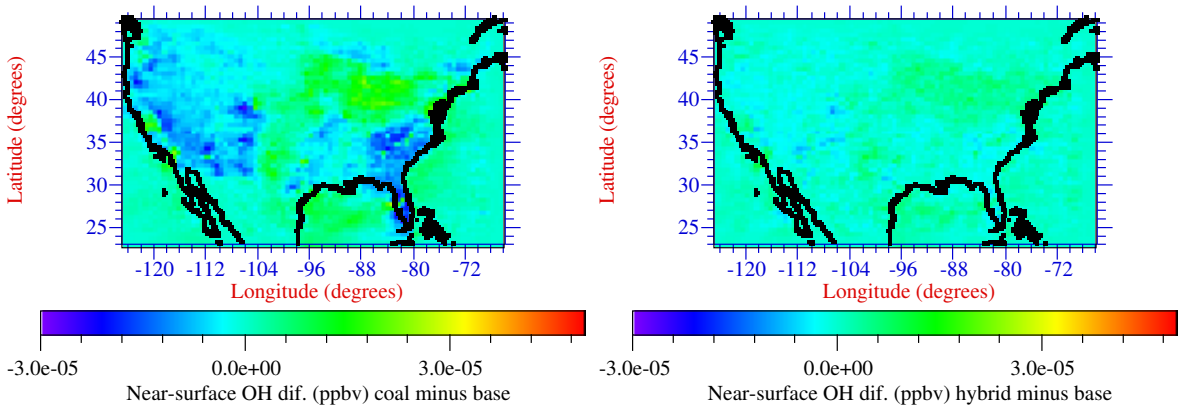

(k) Near-surface black carbon

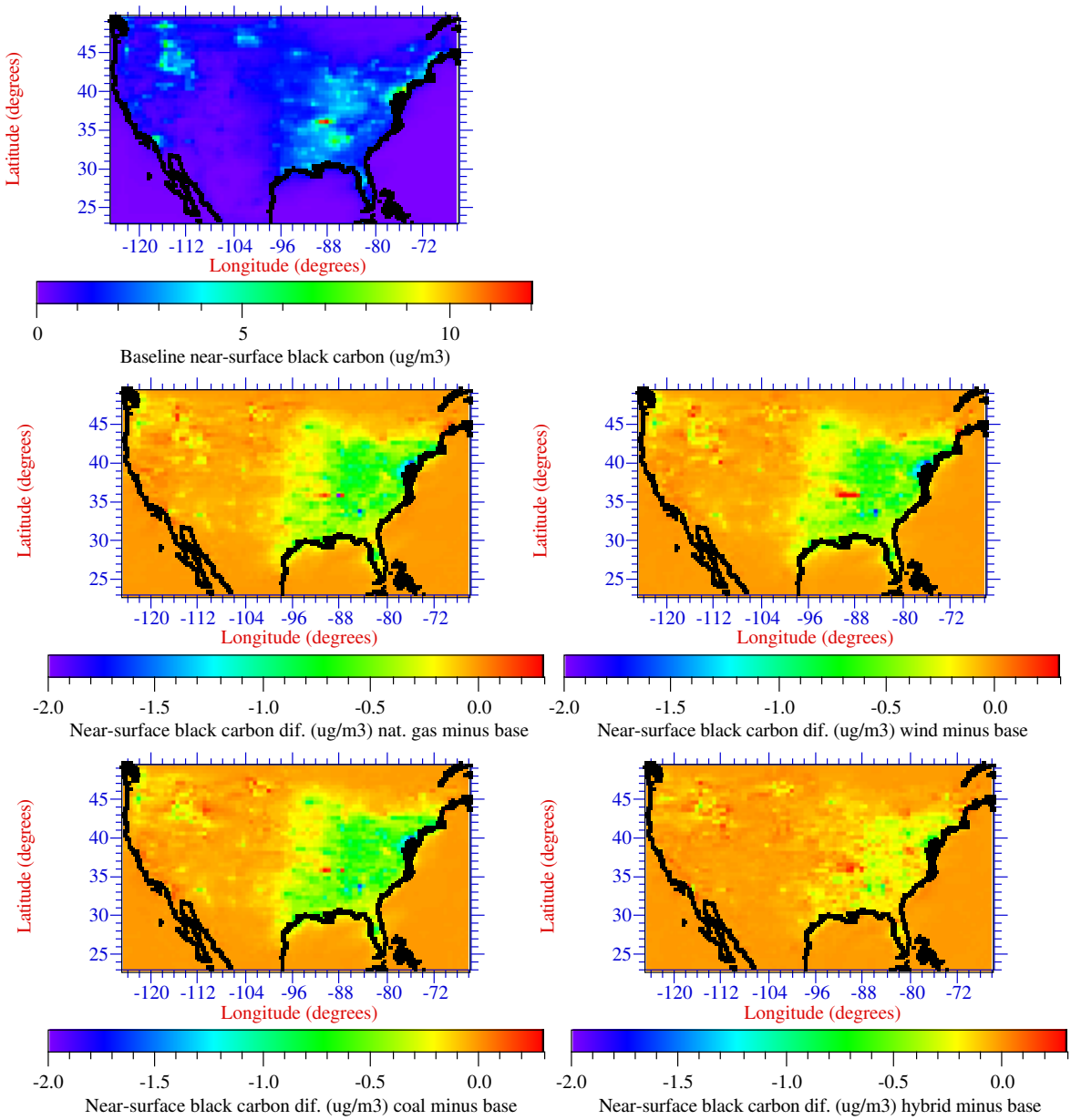

(l) Near-surface particulate nitrate

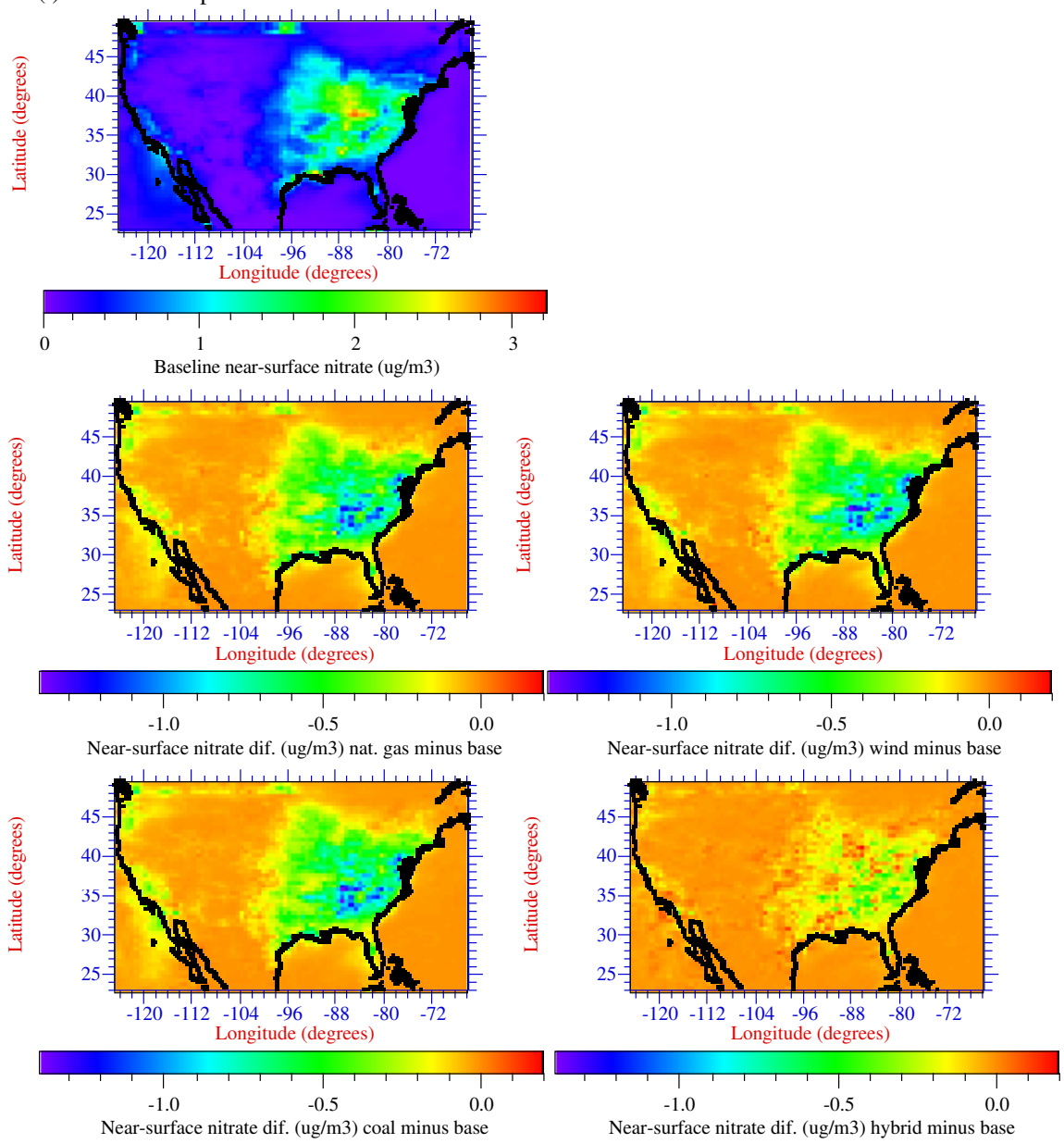

(m) Near-surface particulate sulfate

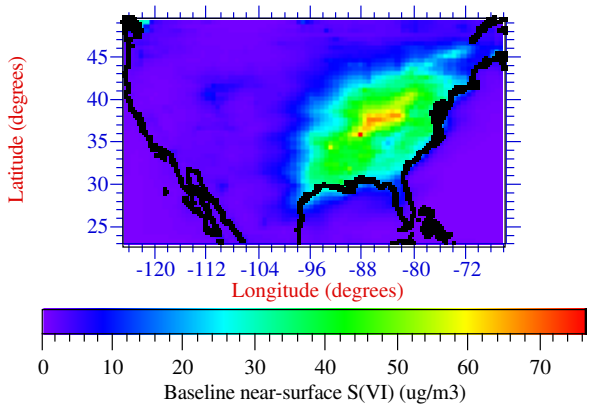

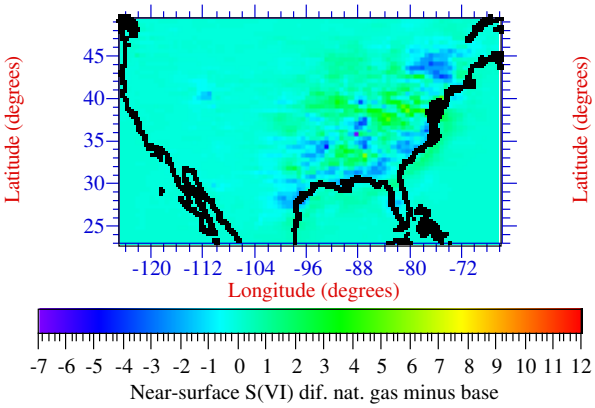

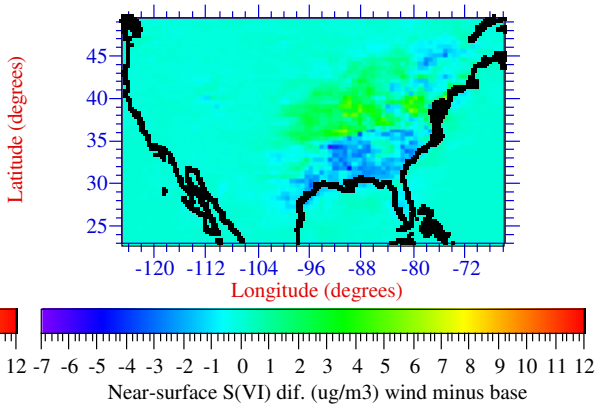

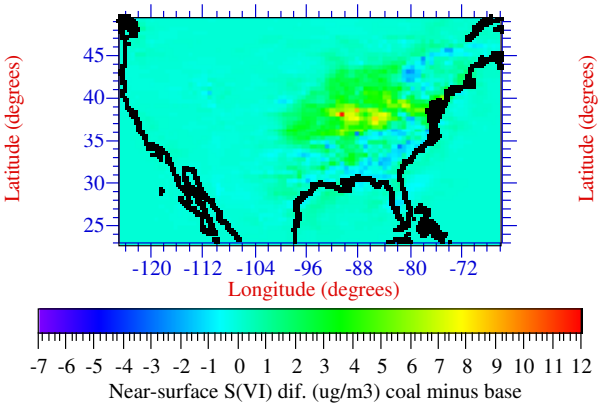

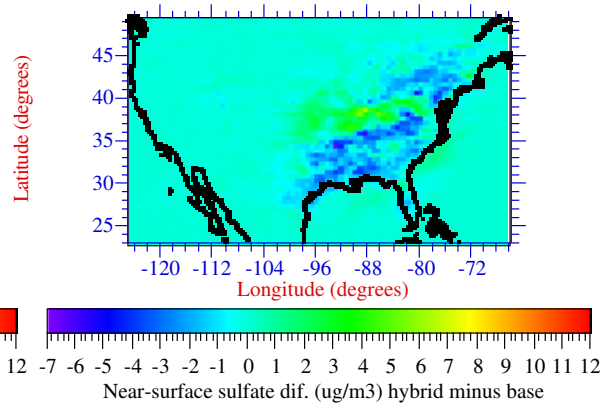

(n) Near-surface water vapor

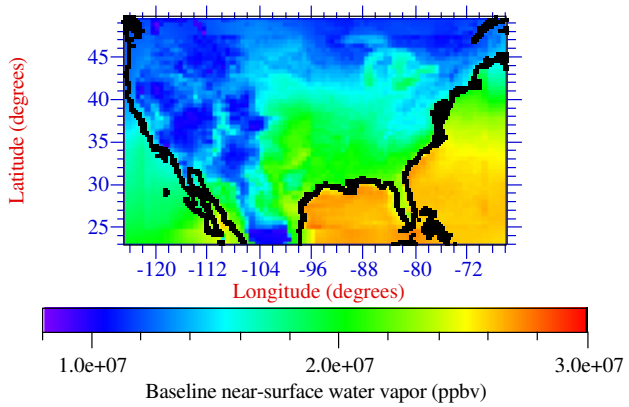

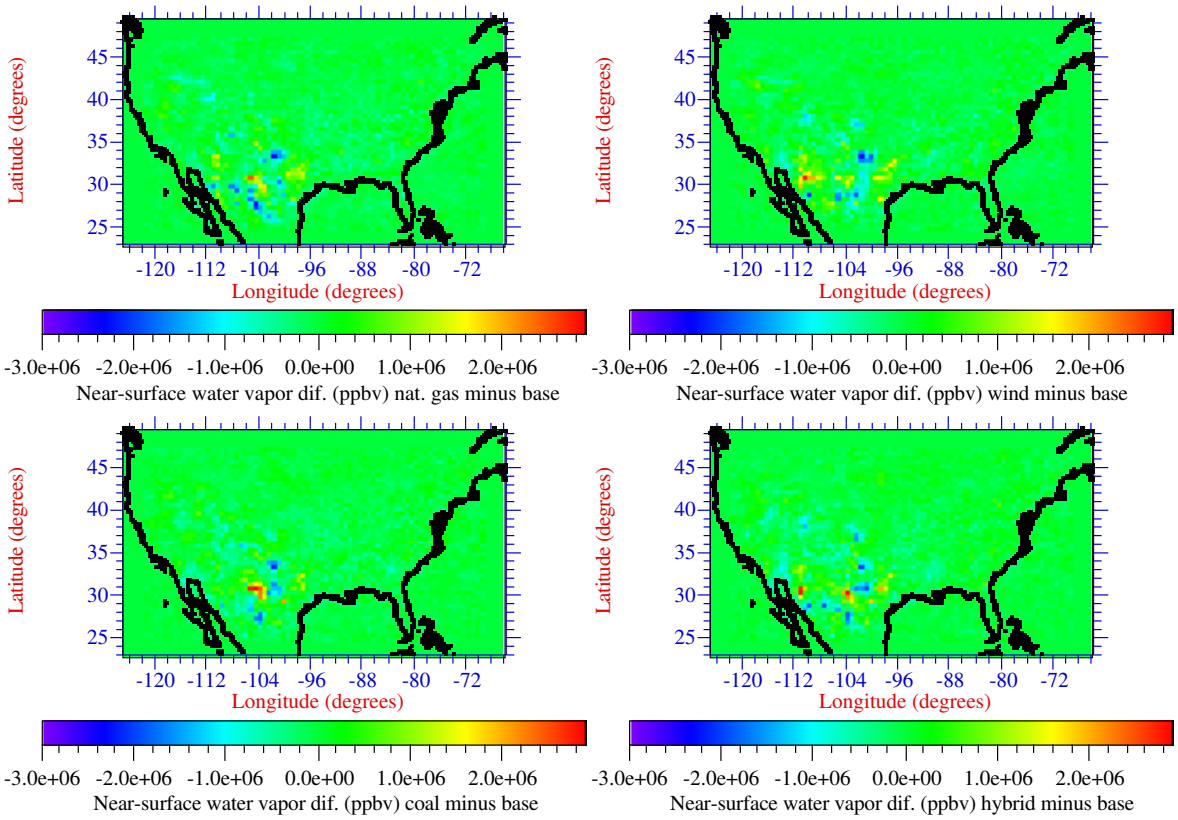

(o) Near-surface methane

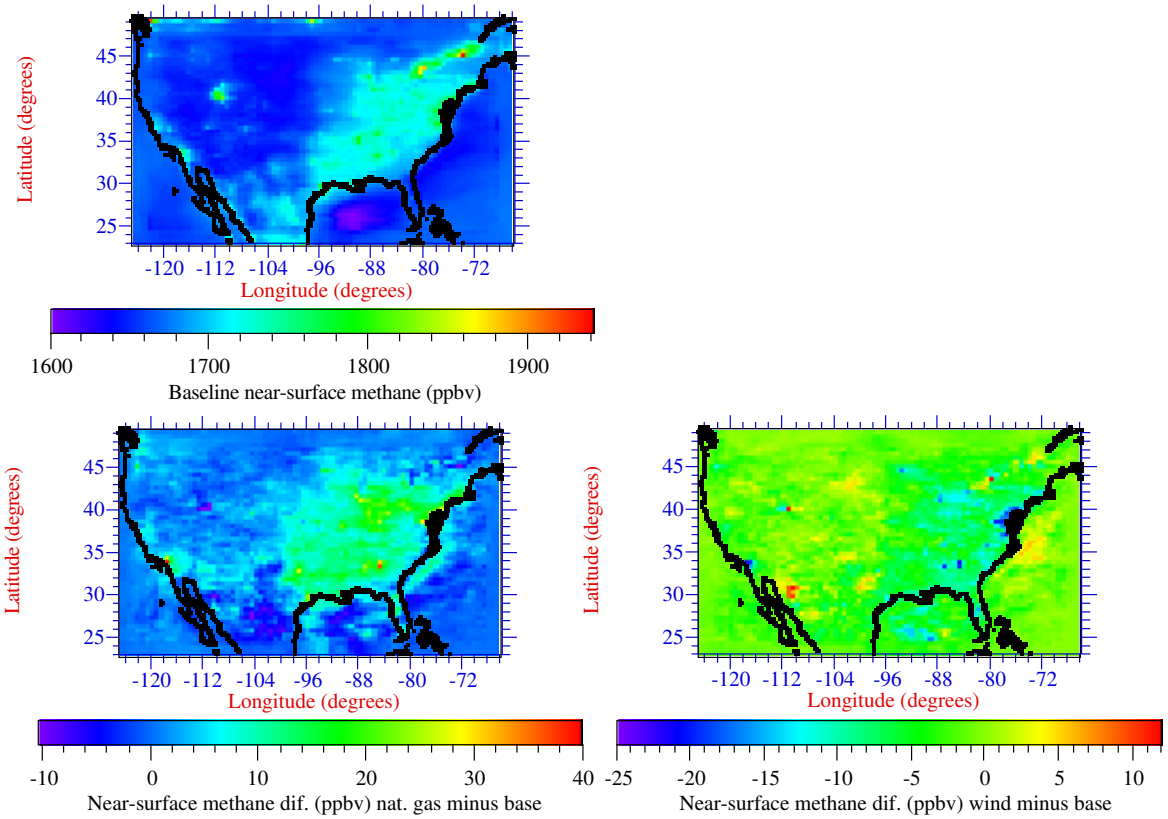

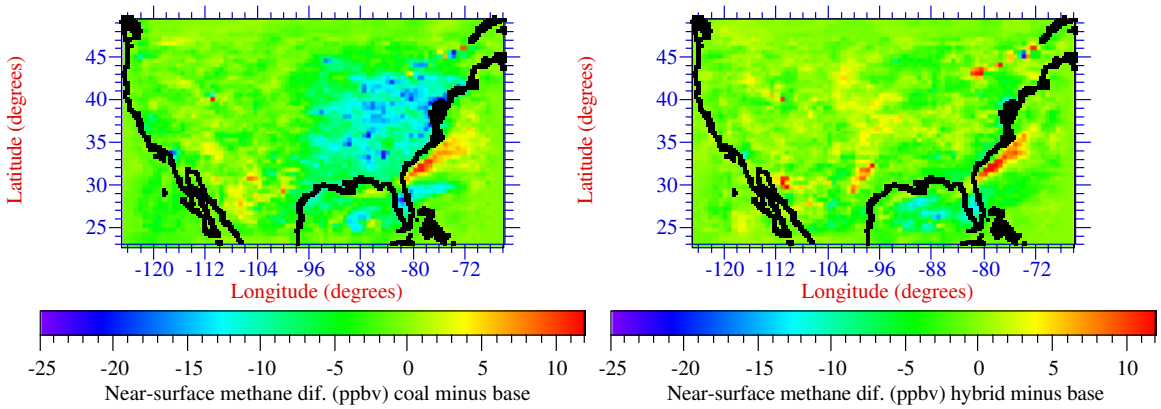

(p) Near-surface carbon dioxide

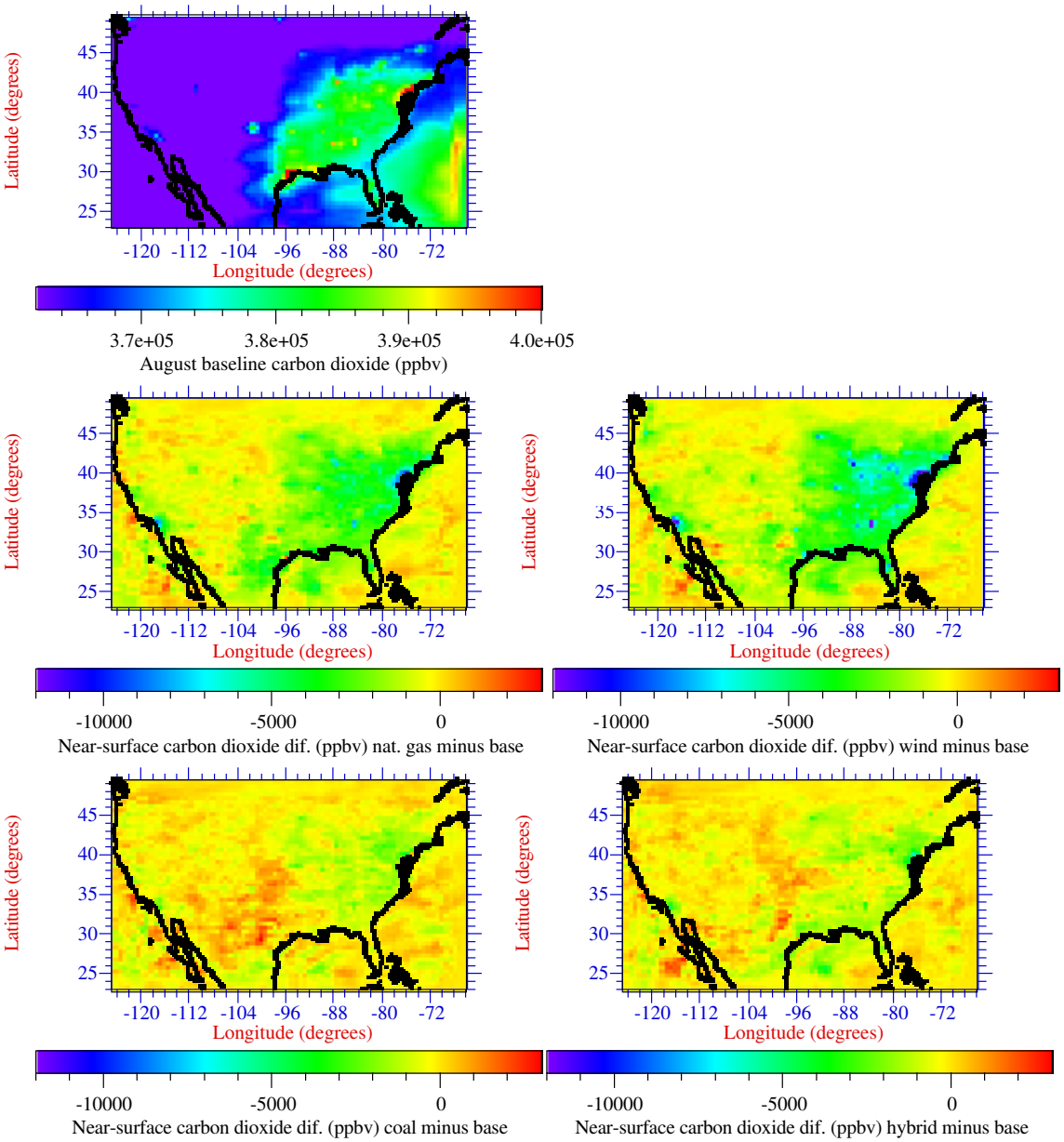

(q) Near-surface molecular hydrogen

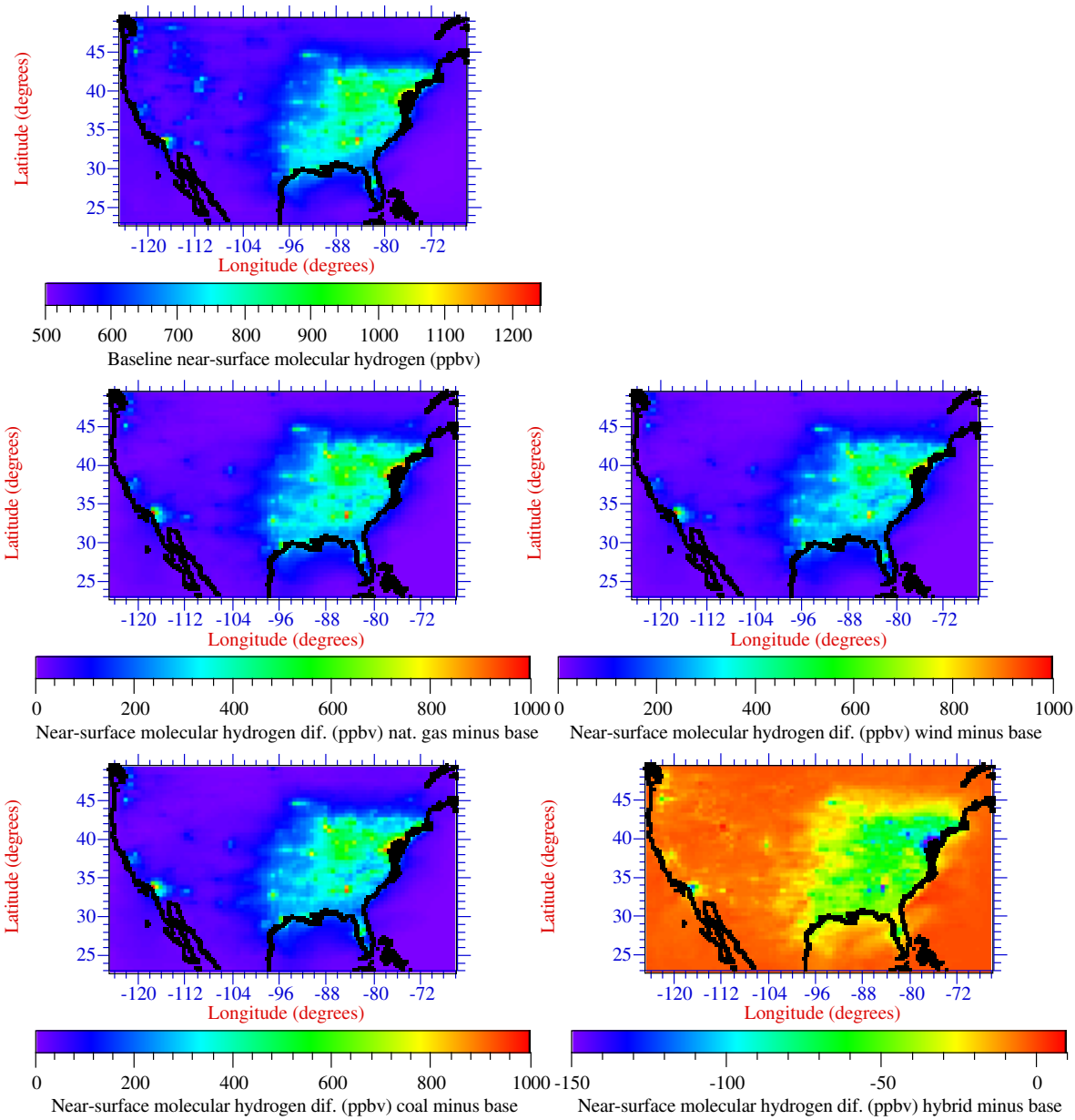

4. Cost analysis of hydrogen generation by wind-electrolysis

Table S2 provides a spreadsheet calculation of low and high estimated near-term (<10 yr) costs of hydrogen from electrolysis, where the electricity is generated by wind. The costs include those for electricity generation, transmission, the electrolyzer, water for the electrolyzer, hydrogen compression, and hydrogen storage. The case assumes that electricity travels by transmission line to filling stations, where electrolyzers produce hydrogen locally, so no transport cost of hydrogen via gas pipeline or truck is necessary.

The wind-electricity costs include the direct cost of wind (turbine, local grid connection, foundation, land, electrical installation, financing, roads, and consultancy) and the long-distance transmission of electricity. The range of $0.03-0.05/kWh in direct wind cost assumes, at the low end, the use of modern turbines in the presence of

sufficiently fast winds. Specifically, the use of a 1.5 MW turbine with a 77-m blade in the presence of 7-7.5 m/s mean annual winds at hub height (80 m) is estimated to give a direct cost of wind electricity (excluding long-distance transmission) of $0.03-0.04/kWh (*S41*). This cost is supported by an analysis of the 25-year real costs of 17 wind farm proposals in California determined as $0.032-$0.037/kWh, with a weighted average of $0.036/kWh (*S42*). The transmission cost of wind is estimated to range from $0.00000345-0.0000138/kWh/km (*S43*), where the high value was derived therein from information in (*S44*). The average distance of transmission lines in the U.S. is assumed to range from 20-1500 km, which should cover all possible *average* distances.

Electrolyzer costs include the costs of purchasing and maintaining the electrolyzer. It is assumed that electricity from wind energy is supplied to each electrolyzer between 50 and 95 percent of the hours of a year. The high end of this range assumes that wind farms are linked together, thereby reducing intermittency and increasing the regularity of wind output (*S45*). The high end also assumes that, at peak wind capacity, more than enough wind-electricity is available for each electrolyzer, with the difference going to the electric grid. Since excess wind-electricity is diverted to the general electric power grid, the extra electric power is not wasted. The lifetime of an electrolyzer is assumed to equal 10 years.

The cost of water for the electrolyzer is assumed to equal $2-$4 per 1000 gallons. The compression estimate includes the cost of electricity for compression. The compression cost estimate appears conservative since the amortized cost of an actual compressor quoted was about $0.45-$0.71/kg-H_2). Storage costs of hydrogen are taken from the literature.

Table S2. Spreadsheet calculation of the estimated low and high cost of producing hydrogen by electrolysis, where the electricity derives from windpower. Values not referenced are either common constants, calculated with the equation given in the first column, or assumed here.

Equation	Parameter (Units)	Low Value	High Value
Energy required to produce hydrogen from 1999 U.S. onroad vehicles			
A^{i}	1999 onroad U.S. vehicle miles traveled (mi/yr)	2.68E+12	2.68E+12
B^{i}	Vehicle fleet mileage (mpg)	17.11	17.11
C=A/B	Gallons of fuel (gas+diesel) used (gal/yr)	1.57E+11	1.57E+11
D	Lower heating value gasoline (MJ/kg)	44	44
E	Gasoline density (kg/m^3)	750	750
F	Gallons per cubic meter (gal/m^3)	264.17287	264.17287
G=D*E/F	Energy stored in gasoline (MJ/gal)	124.9182022	124.918202
H=C*G	Energy required to power gasoline vehicles (MJ/yr)	1.96E+13	1.96E+13
I^{i}	Gasoline vehicle efficiency (fraction)	0.16	0.16
J=H*I	Actual energy required for vehicles (MJ/yr)	3.14E+12	3.14E+12
K^{i}	HFCV efficiency (fraction)	0.46	0.43
L=J/K	Energy required for HFCV (MJ/yr)	6.82E+12	7.29E+12
M	Lower heating value of hydrogen (MJ/kg-H_2)	119.96	119.96
N=L/M	Mass of H_2 required for fuel (kg-H_2/yr)	5.68E+10	6.08E+10
O	Leakage rate of hydrogen (fraction)	0.03	0.1
P=N/(1-O)	Mass of H_2 required with max leakage (kg-H_2/yr)	58582623448	6.7544E+10
Q	Higher heating value of hydrogen (MJ/kg-H_2)	141.8	141.8
R=P*Q	Energy to produce HFCV+leaked H_2 (MJ/yr)	8.30702E+12	9.5778E+12
S=R/3.6	Energy to produce HFCV+leaked H_2 (kWh/yr)	2.3075E+12	2.6605E+12
Cost of electricity from wind for electrolysis			
T^{ii}	Direct, unsubsidized wind electricity cost ($/kWh)	0.03	0.05

U[iii]	Transmission cost of wind ($/kWh/km)	0.00000345	0.0000138
V	Length of average transmission line (km)	20	1500
W=U*V	Transmission cost of wind ($/kWh)	0.000069	0.0207
X=T+W	Direct+transmission cost of wind ($/kWh)	0.030069	0.0707
Y[vii]	Electrolyzer efficiency for producing hydrogen	0.738	0.738
Z=S*X/Y	Cost of electricity to generate H_2 ($/yr)	94016736018	2.5487E+11
a=Z/P	Cost of electricity per mass of H_2 ($/kg-$H_2$)	1.604857046	3.77343421
Cost of electrolyzer			
b[iv]	Electrolyzer cost (including installation) ($/kW)	400	1000
c[v]	Fraction of time electrolyzer used	0.95	0.5
d=10yr[vi]	Electrolyzer lifetime (yr)	10	10
e	Interest rate	0.06	0.08
f=e/(1-1/(1+e)^d)	Annual payment factor	0.135867958	0.14902949
g=b*f	Annual cost of purchasing electrolyzer ($/kW/yr)	54.34718329	149.029489
h=b*0.015[vi]	Annual O&M (1.5% of purchase cost) ($/kW/yr)	6	15
i=g+h	Total annual cost of electrolyzer ($/kW/yr)	60.34718329	164.029489
j[vii]	Actual electrolyzer energy requirement (kWh/kg-H_2)	53.4	53.4
k	kWh/yr per kW	8760	8760
l=k*c	kWh/yr actually used per rated kW	8322	4380
m=I*j/k	Cost of electrolysis for producing H_2 ($/kg-$H_2$)	0.387231385	1.99981157
Cost of water for electrolysis			
n	H_2 molecular weight (g/mol)	2.0158	2.0158
o	H_2O molecular weight (g/mol)	18.015	18.015
p=o/n	Water required for electrolyzer (kg-H_2O/kg-H_2)	8.936898502	8.9368985
q	Density of liquid water (kg/m^3)	1000	1000
r=p*F/q	Water required for electrolyzer (gal-H_2O/kg-H_2)	2.360886126	2.36088613
s	Cost of water per gallon ($/gal-$H_2O$)	0.002	0.004
t=r*s	Cost of water per kg-H_2 ($/kg-$H_2$)	0.004721772	0.00944354
Cost of compressor			
u[vi,viii]	Cost of H_2 compression ($/kg-$H_2$)	0.7	1.34
Cost of storage			
v[vi]	Cost of H_2 storage ($/kg-$H_2$)	0.31	0.31
Total cost			
w=a+m+t+u+v	Total cost ($/kg-$H_2$)	3.00681009	7.4326891
x=w*P/C	Total cost per displaced gallon ($/gal)	1.12E+00	3.20E+00

Sources: (i) (*S1*) and references therein; (ii) (*S41*), (*S42*); (iii) (*S43*); (iv) (*S46*); (v) the high estimate assumes that multiple connected wind farms reduce intermittency (*S45*), and a larger wind capacity than necessary is assigned to each electrolyzer, with the remainder going to electricity, (vi) (*S47*); (vii) (*S48*); (viii) (*S49*).

5. Estimate of the Global Warming Potential of BC+OM and of SO_x.

The 100-year climate response ratio, defined here as the climate response per unit anthropogenic emission of a substance relative to that of anthropogenic CO_2 is a parameter analogous to a global warming potential, GWP, but calculated in terms of globally-averaged temperature change rather than radiative forcing. The 100-yr climate response ratio of fossil-fuel black carbon plus organic matter (BC+OM) is calculated here as follows. The modeled temperature change resulting from eliminating anthropogenic CO_2, assuming a yearly fossil-fuel plus net anthropogenic biomass-burning emission rate

of 8100 Tg-C/yr in Figure 10 of (*S13*) was -1 K for a CO_2 lifetime of 30 yr and -2 K for a lifetime of 95 yr. The 100-yr temperature change due to eliminating a yearly emission of 4.9 Tg-C/yr BC plus 8.7 Tg-C/yr OM (*S13*, paragraph 19] for a total of 13.6 Tg-C/yr BC+OM was -0.32 K (*S13*, Figure 10). The calculations for those studies accounted for many feedbacks of gases and aerosol particles to climate. Dividing the temperature change per unit emission of BC+OM to that of CO_2 gives a climate response ratio for BC+OM of 95 to 191.

The 100-year climate response ratio of SO_x is estimated as follows. The climate response of eliminating 145 Tg-SO_2/yr (anthropogenic) from paragraph 63 of (*S11*) was +0.7 K. Dividing the climate response per unit emission of SO_2 to that of CO_2 from the previous paragraph gives a climate response ratio for SO_x of -19.5 to –39.

Acknowledgments

Support for researchers on and equipment for this project came from Stanford University's Global Climate and Energy Project and the National Aeronautics and Space Administration. We would like to thank Jon Koomey and Mark Delucchi for helpful comments.

References

S1. Colella, W.G., M.Z. Jacobson, and D.M. Golden, Switching to a U.S. hydrogen fuel cell vehicle fleet: The resultant change in emissions, energy use, and global warming gases, *Journal of Power Sources*, in press, 2005.

S2. Jacobson, M. Z., Development and application of a new air pollution modeling system. Part II: Aerosol module structure and design, *Atmos. Environ*., *31A*, 131-144, 1997.

S3. Jacobson, M. Z., Development and application of a new air pollution modeling system. Part III: Aerosol-phase simulations, *Atmos. Environ*., *31A*, 587-608, 1997.

S4. Jacobson, M. Z., Studying the effects of aerosols on vertical photolysis rate coefficient and temperature profiles over an urban airshed, *J. Geophys. Res*., *103*, 10,593-10,604, 1998.

S5. Jacobson, M. Z., Isolating nitrated and aromatic aerosols and nitrated aromatic gases as sources of ultraviolet light absorption, *J. Geophys. Res.*, *104*, 3527-3542, 1999.

S6. Jacobson, M. Z., GATOR-GCMM: A global through urban scale air pollution and weather forecast model. 1. Model design and treatment of subgrid soil, vegetation, roads, rooftops, water, sea ice, and snow., *J. Geophys. Res*., *106*, 5385-5402, 2001.

S7. Jacobson, M. Z., GATOR-GCMM: 2. A study of day- and nighttime ozone layers aloft, ozone in national parks, and weather during the SARMAP Field Campaign, *J. Geophys. Res*., *106*, 5403-5420, 2001.

S8. Jacobson, M. Z., J. H. Seinfeld, G. R. Carmichael, and D.G. Streets, The effect on photochemical smog of converting the U.S. fleet of gasoline vehicles to modern diesel vehicles, *Geophys. Res. Lett.*, *31*, L02116, doi:10.1029/2003GL018448, 2004.

S9. Jacobson, M.Z., and J.H. Seinfeld, Evolution of nanoparticle size and mixing state near the point of emission, *Atmos. Environ*., 38, 1839-1850, 2004.

S10. Jacobson, M. Z., Strong radiative heating due to the mixing state of black carbon in atmospheric aerosols, *Nature*, *409*, 695-697, 2001.

S11. Jacobson, M. Z., Control of fossil-fuel particulate black carbon plus organic matter, possibly the most effective method of slowing global warming, *J. Geophys. Res., 107*, (D19), 4410, doi:10.1029/2001JD001376, 2002.

S12. Jacobson, M. Z., The short-term cooling but long-term global warming due to biomass burning, *J. Clim*., 17 (15), 2909-2926, 2004.

S13. Jacobson, M.Z., The climate response of fossil-fuel and biofuel soot, accounting for soot's feedback to snow and sea ice albedo and emissivity, *J. Geophys. Res*., *109*, doi:10.1029/2004JD004945, 2004b.

S14. Arakawa, A., and V. R. Lamb, A potential enstrophy and energy conserving scheme for the shallow water equations, *Mon. Wea. Rev*., *109*, 18-36, 1981.

S15. Lu, R., and R. P. Turco, Air pollutant transport in a coastal environment, II, Three-dimensional simulations over Los Angeles basin, *Atmos. Environ*., *29*, 1499-1518, 1995.

S16. Walcek, C. J., and N. M. Aleksic, A simple but accurate mass conservative, peak-preserving, mixing ratio bounded advection algorithm with fortran code, *Atmos. Environ*., *32*, 3863-3880, 1998.

S17. Jacobson, M. Z., Improvement of SMVGEAR II on vector and scalar machines through absolute error tolerance control. Atmos. Environ., 32, 791–796, 1998.

S18. Jacobson, M. Z., *Fundamentals of Atmospheric Modeling*. Cambridge University Press, New York, 656 pp., 1999.

S19. Sander, S.P., R.R. Friedl, WB. DeMore, DM. Golden, M.J. Kurylo, R.F. Hampson, R.E. Huie, G.K. Moortgat, A.R. Ravishankara, C.E. Kolb, and M.J. Molina, Chemical kinetics and photochemical data for use in stratospheric modeling. Supplement to Evaluation 12, JPL Publ. 00-3, Jet Propulsion Laboratory, Pasadena, CA, 2000.

S20. Jacobson, M. Z., Analysis of aerosol interactions with numerical techniques for solving coagulation, nucleation, condensation, dissolution, and reversible chemistry among multiple size distributions, *J. Geophys. Res*., *107* (D19), 4366, doi:10.1029/ 2001JD002044, 2002.

S21. Jacobson, M. Z., Development of mixed-phase clouds from multiple aerosol size distributions and the effect of the clouds on aerosol removal, *J. Geophys. Res*., *108* (D8), 4245, doi:10.1029/2002JD002691, 2003.

S22. Vehkamaki, H., M. Kulmala, I. Napari, K.E.J. Lehtinen, C. Timmreck, M. Noppel, and A. Laaksonen, An improved parameterization for sulfuric acid-water nucleation rates for tropospheric and stratospheric conditions, *J. Geophys. Res., 107* (D22), 4622, doi:10.1029/2002JD002184, 2002.

S23. Jacobson, M.Z., A solution to the problem of nonequilibrium acid/base gas-particle transfer at long time step, *Aerosol Sci. Technol, 39*, 92-103, 2005.

S24. Jacobson, M. Z., Studying The effects of calcium and magnesium on size-distributed nitrate and ammonium with EQUISOLV II, *Atmos. Environ., 33*, 3635-3649, 1999.

S25. Mellor, G. L., and T. Yamada, Development of a turbulence closure model for geophysical fluid problems, *Revs. of Geophys. and Space Phys*., *20*, 851-875, 1982.

S26. Ding, P., and D. A. Randall, A cumulus parameterization with multiple cloud-base levels, *J. Geophys. Res*., *103*, 11,341-11,353, 1998.

S27. Toon, O. B., C. P. McKay, T. P. Ackerman, and K. Santhanam, Rapid calculation of radiative heating rates and photodissociation rates in inhomogeneous multiple scattering atmospheres, *J. Geophys. Res*., *94,* 16,287-16,301, 1989.

S28. Jacobson, M.Z., A refined method of parameterizing absorption coefficients among multiple gases simultaneously from line-by-line data, *J. Atmos. Sci., 62*, 506-517, 2005.

S29. Toon, O. B., and T. P. Ackerman, Algorithms for the calculation of scattering by stratified spheres, *Appl. Opt*., *20*, 3657-3660, 1981.

S30. Grenfell, T.C., and S.G. Warren, Representation of a nonspherical ice particle by a collection of independent spheres for scattering and absorption of radiation, *J. Geophys. Res*., *104*, 31,697-31,709, 1999.

S31. Ketefian, G., and M. Z. Jacobson, Development and application of a 2-D potential-enstrophy-, energy-, and mass-conserving mixed-layer ocean model with arbitrary boundaries, in review, 2005.

S32. Jacobson, M.Z., Studying ocean acidification with conservative, stable numerical schemes for nonequilibrium air-ocean exchange and ocean equilibrium chemistry, *J. Geophys. Res*., *110*, doi:10.1029/2004JD005220, 2005c, www.stanford.edu/group/efmh/jacobson/oceanAcidif.html.

S33. United States Environmental Protection Agency (USEPA). Clearinghouse for Inventories and Emission Factors, http://www.epa.gov/ttn/chief/, 2003.

S34. United States Environmental Protection Agency (USEPA). Improvements in Vegetation Cover Data, http://www.epa.gov/AMD/beld3.html, 2003.

S35. United States Geological Survey (USGS) / U. Nebraska, Lincoln / European Commission's Joint Research Center. 1-km resolution global landcover characteristics data base, derived from Advanced Very High Resolution Radiometer (AVHRR) data from the period April 1992 to March 1993, 1999.

S36. Guenther, A., et al., A global model of natural volatile organic compound emissions, *J. Geophys. Res*., *100*, 8873-8892, 1995.

S37. Bond, T.C., Streets, D.G., Yarber, K.F., Nelson, S.M., Woo, J.-H. & Klimont, Z., A technology-based global inventory of black and organic carbon emissions from combustion, *J. Geophys. Res*., 109, D14203, doi: 10.1029/2003JD003697, 2004.

S38. National Center for Environmental Prediction (NCEP), 2.5 degree global final analyses, distributed by the Data Support Section, National Center for Atmospheric Research, 2003.

S39. United States Environmental Protection Agency (USEPA). AIR Data, http://www.epa.gov/air/data/, 2003.

S40. Barnes, D.H., S.C. Wofsy, B.P. Fehlau, E.W. Gottlieb, J.W. Elkins, G.S. Dutton, and P.C. Novelli, Hydrogen in the atmosphere: Observations above a forest canopy in a polluted environment, *J. Geophys. Res., 108* (D6), 4197, doi:10.1029/2001JD001199, 2003.

S41. Jacobson, M.Z., and G.M. Masters, Exploiting wind versus coal, *Science*, *293*, 1438, 2001a.

S42. Bolinger, M., and R. Wiser, Summary of Power Authority Letters of Intent for Renewable Energy, Memorandum, Lawrence Berkeley National Laboratory, Oct. 30, 2001, 2001.

S43. Jacobson, M.Z., and G.M. Masters, dEbate Response to Alfred Cavallo letter of November 21, 2004," *Science*, www.sciencemag.org/cgi/eletters/294/5544/1000, 2001.

S44. Cavallo, A.J., High-capacity factor wind energy systems, *JSEE 117*, 137, 1995.

S45. Archer, C. L., and M. Z. Jacobson, Spatial and temporal distributions of U.S. winds and wind power at 80 m derived from measurements, *J. Geophys. Res*., 108 (*D9*) 4289, doi:10.1029/2002JD002076, 2003.

S46. National Academy of Science (NAS), The hydrogen economy: opportunities, costs, barriers, and R&D needs, National Academies Press, Washington D.C., p. 3-3, 2004.

S47. Lee, K., Economic feasibility of producing hydrogen using excess electricity from wind turbines on the Big Island of Hawaii, World Renewable Energy Cong. VIII, Denver, Colo., Sept. 3, 2004, www.sentech.org/Lee,%20K_Economic%20Feasibility%20Hawaii.pdf, 2004.

S48. National Renewable Energy Laboratory (NREL), Technology Brief: Analysis of current-day commercial electrolyzers, NREL/FS-560-36705, Sept. 2004, 2004.

S49. Myers, D.B., G.D. Ariff, R.C. Kuhn, and B.D. James, Hydrogen from renewable energy sources: Pathway to 10 quads for transportation uses in 2030 to 2050., FY 2003 Progress Report, http://www.eere.energy.gov/hydrogenandfuelcells, 2003.